The Astrophysical Journal, 814:127 (17pp), 2015 December 1 doi:10.1088/0004-637X/814/2/127

POLARIZED SCATTERING OF LIGHT FOR ARBITRARY MAGNETIC FIELDS WITH LEVEL-CROSSINGS FROM THE COMBINATION OF HYPERFINE AND FINE STRUCTURE SPLITTINGS

K. Sowmya[1], K. N. Nagendra[1], M. Sampoorna[1], and J. O. Stenflo[2,3]
[1] Indian Institute of Astrophysics, Koramangala, Bengaluru, India; ksowmya@iiap.res.in, knn@iiap.res.in, sampoorna@iiap.res.in
[2] Institute of Astronomy, ETH Zurich, CH-8093 Zurich, Switzerland; stenflo@astro.phys.ethz.ch
[3] Istituto Ricerche Solari Locarno, Via Patocchi, 6605 Locarno-Monti, Switzerland
Received 2015 April 3; accepted 2015 October 6; published 2015 November 25

ABSTRACT

Interference between magnetic substates of the hyperfine structure states belonging to different fine structure states of the same term influences the polarization for some of the diagnostically important lines of the Sun's spectrum, like the sodium and lithium doublets. The polarization signatures of this combined interference contain information on the properties of the solar magnetic fields. Motivated by this, in the present paper, we study the problem of polarized scattering on a two-term atom with hyperfine structure by accounting for the partial redistribution in the photon frequencies arising due to the Doppler motions of the atoms. We consider the scattering atoms to be under the influence of a magnetic field of arbitrary strength and develop a formalism based on the Kramers–Heisenberg approach to calculate the scattering cross section for this process. We explore the rich polarization effects that arise from various level-crossings in the Paschen–Back regime in a single scattering case using the lithium atomic system as a concrete example that is relevant to the Sun.

Key words: atomic processes – line: formation – polarization – scattering – Sun: magnetic fields

1. INTRODUCTION

In the present paper, we address the problem of quantum interference between the magnetic substates of the hyperfine structure (F) states pertaining to different fine structure (J) states of a given term, in the presence of magnetic fields of arbitrary strength covering the Hanle, Zeeman, and Paschen–Back (PB) effect regimes. We will refer to this as "combined interference" or the "$F+J$ state interference." We develop the necessary theory including the effects of partial frequency redistribution (PRD) in the absence of collisions, assuming the lower levels to be unpolarized and infinitely sharp. We refer to this theory as the "combined theory" throughout the paper.

We consider a two-term atom with hyperfine structure under the assumption that the lower term is unpolarized. In the absence of a magnetic field, the atomic transitions in a two-term atom take place between the degenerate magnetic substates belonging to the F states. An applied magnetic field lifts the degeneracies and modifies the energies of these magnetic substates. The amount of splitting (or the energy change) produced by the magnetic field defines the regimes in which Zeeman and PB effects act. Depending on the relative magnitudes of the fine structure splitting (FS), the hyperfine structure splitting (HFS), and the magnetic splitting (MS), we characterize the magnetic field strength into five regimes. These regimes are illustrated schematically in Figure 1. In the approach presented in this paper, we account for the interferences between the magnetic substates pertaining to the same F state, the magnetic substates belonging to different F states of the same J state, and the magnetic substates belonging to different F states pertaining to different J states. Although all three types of interference are always present, depending on the field strength one or two of them would dominate as depicted in the different panels of Figure 1.

Within the framework of non-relativistic quantum electrodynamics, Casini & Manso Sainz (2005) formulated a theory for polarized scattering on a multi-term atom with hyperfine structure in the presence of an arbitrary strength magnetic field under the approximation of complete frequency redistribution (CRD). In the present paper, we restrict our treatment to a two-term atom with HFS and consider the limit of coherent scattering in the atomic frame with Doppler frequency redistribution in the observer's frame. We base our formalism on the Kramers–Heisenberg coherency matrix approach of Stenflo (1994). In our combined theory, we do not account for the coherences among the states in the lower term. In a recent paper, Stenflo (2015) indicated how they may be included by extending the coherency matrix approach to the multi-level case.

Based on the concept of "metalevels," Landi Degl'Innocenti et al. (1997) formulated a theory that is able to treat coherent scattering in the atomic rest frame for a two-term atom with hyperfine structure. Recently, Casini et al. (2014) presented a generalized frequency redistribution function for the polarized two-term atom in arbitrary fields, based on a new formulation of the quantum scattering theory. Our approach is an alternative approach to the same problem and is conceptually more transparent, although limited to infinitely sharp and unpolarized lower levels.

Belluzzi et al. (2009) studied the linear polarization produced due to scattering on the D lines of neutral lithium isotopes. They employed the density matrix formalism of Landi Degl'Innocenti & Landolfi (2004, hereafter LL04), together with the approximation of CRD, to treat the quantum interference between the fine and hyperfine structure states. They restricted their study to the non-magnetic case. However, they explored the sensitivity of the Stokes profiles to the microturbulent magnetic fields. For our study in the present paper, we consider the same D lines of lithium isotopes and present in detail the effects of a deterministic magnetic field of arbitrary strength. For this atomic line system, the PB effect in both the fine and the hyperfine structure states occurs for the magnetic field strengths encountered on the Sun. We restrict our treatment to the single scattering case, since our aim here is to explore the basic physical effects of the combined theory.

2. THE ATOMIC MODEL

In this section, we describe the structure of the model atom considered for our studies and its interaction with an external magnetic field. We consider a two-term atom, each state of which is designated by the quantum numbers L (orbital), S (electron spin), J ($=L+S$), I_s (nuclear spin), F ($=J+I_s$), and μ (projection of F onto the quantization axis).

2.1. The Atomic Hamiltonian

Under the L–S coupling scheme, the atomic Hamiltonian for a two-term atom with hyperfine structure is given by

$$\mathcal{H}_A = \zeta(LS)\boldsymbol{L}\cdot\boldsymbol{S} + \mathcal{A}_J\boldsymbol{I}_s\cdot\boldsymbol{J} + \frac{\mathcal{B}_J}{2I_s(2I_s-1)J(2J-1)} \times\left\{3(\boldsymbol{I}_s\cdot\boldsymbol{J})^2+\frac{3}{2}(\boldsymbol{I}_s\cdot\boldsymbol{J})-I_s(I_s+1)J(J+1)\right\}, \quad (1)$$

where $\zeta(LS)$ is a constant having the dimensions of energy, and $\mathcal{A}_J$ and $\mathcal{B}_J$ are the magnetic dipole and electric quadrupole hyperfine structure constants, respectively. The first term in the above equation is a measure of the FS while the second and the third terms provide a measure of the HFS. The eigenvalues of the atomic Hamiltonian represent the energies of the F states, calculated with respect to the energy of the corresponding term.

2.2. The Magnetic and the Total Hamiltonians

An external magnetic field lifts the degeneracies of the magnetic substates of the F states and changes their energies by an amount given by the eigenvalues of the magnetic Hamiltonian

$$\mathcal{H}_B = \mu_0(\boldsymbol{J}+\boldsymbol{S})\cdot\boldsymbol{B}. \quad (2)$$

Assuming the quantization axis to be along the magnetic field (z-axis of the reference system), the matrix elements of the total Hamiltonian, $\mathcal{H}_T = \mathcal{H}_A + \mathcal{H}_B$, can be written as

$$\begin{aligned}\langle LSJI_sF\mu|\mathcal{H}_T|LSJ'I_sF'\mu\rangle &= \delta_{JJ'}\delta_{FF'}\\ &\times\left[\frac{1}{2}\zeta(LS)\{J(J+1)-L(L+1)-S(S+1)\}\right.\\ &+\frac{1}{2}\mathcal{A}_J\mathcal{K}+\frac{\mathcal{B}_J}{8I_s(2I_s-1)J(2J-1)}\\ &\times\left.\{3\mathcal{K}(\mathcal{K}+1)-4J(J+1)I_s(I_s+1)\}\right]\\ &+\mu_0B(-1)^{L+S+J+J'+I_s-\mu+1}\\ &\times\sqrt{(2J+1)(2J'+1)(2F+1)(2F'+1)}\\ &\times\begin{pmatrix}F & F' & 1\\ -\mu & \mu & 0\end{pmatrix}\begin{Bmatrix}J & J' & 1\\ F' & F & I_s\end{Bmatrix}\\ &\times\left[\delta_{JJ'}(-1)^{L+S+J+1}\frac{\sqrt{J(J+1)}}{\sqrt{2J+1}}\right.\\ &+\left.(-1)^{J-J'}\sqrt{S(S+1)(2S+1)}\begin{Bmatrix}J & J' & 1\\ S & S & L\end{Bmatrix}\right], \quad (3)\end{aligned}$$

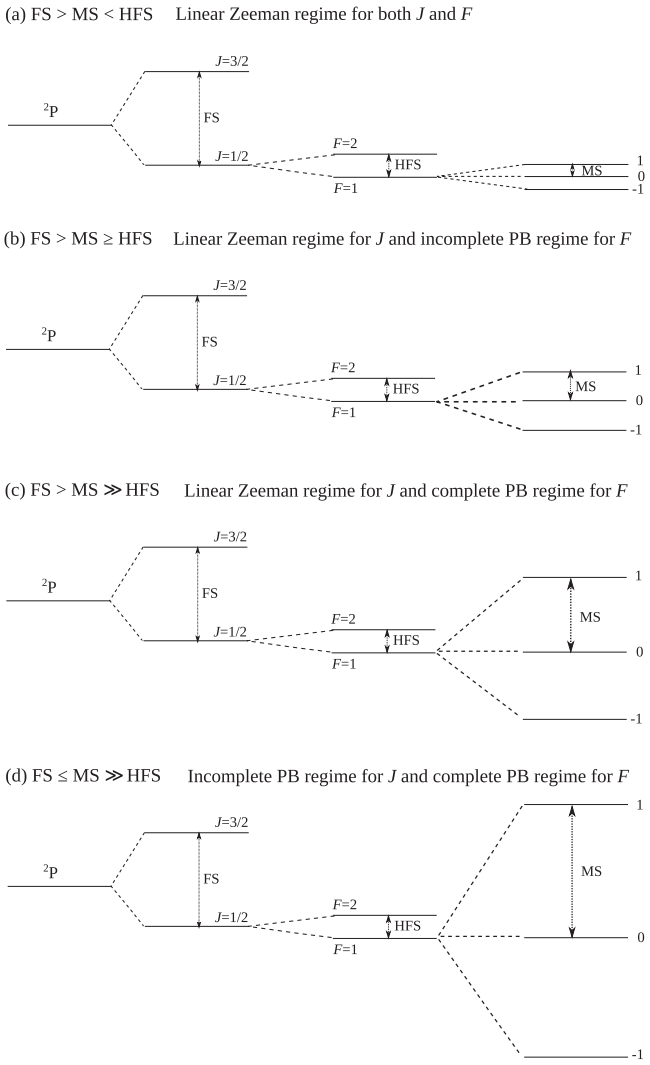

Figure 1. Illustration of the magnetic field strength regimes in the combined theory. For illustration purposes, a ^{2}P term with nuclear spin $3/2$ is considered. The various splittings indicated are not to scale. Panels (a)–(d) show the first four regimes of the field strength. When MS is much greater than FS, we have a complete PB regime for both J and F, which we call the fifth regime (not illustrated in the figure).

where $\mathcal{K} = F(F+1) - I_s(I_s+1) - J(J+1)$, and μ_0 is the Bohr magneton. The total Hamiltonian matrix in the combined theory is no longer a symmetric tridiagonal matrix, unlike the case of the PB effect in fine or hyperfine structure states. Instead, it is a full symmetric matrix and we diagonalize it using the Givens–Householder method described in Ortega (1968). We test the diagonalization code written for the problem at hand using the principle of spectroscopic stability (PSS) presented in Appendix B.

2.3. Eigenvalues and Eigenvectors

The diagonalization of the total Hamiltonian gives the energy eigenvectors in terms of the linear Zeeman effect regime basis $|LSJI_sF\mu\rangle$ through the expansion coefficients C^k_{JF} as

$$|LSI_s,\, k\mu\rangle = \sum_{JF} C^k_{JF}(LSI_s,\,\mu)\,|LSJI_sF\mu\rangle. \quad (4)$$

The symbol k labels different states corresponding to the given values of (L, S, I_s, μ) and its dimension is given by

$$N_k = \sum_{d=|L-S|}^{L+S} 1 + d + I_s - \max\left(|\mu|, \left|d - I_s\right|\right). \quad (5)$$

We assume the C-coefficients appearing in Equation (4) to be real because the total Hamiltonian is real. We obtain the C-coefficients and the corresponding eigenvalues denoted here as $E_k(LSI_s, \mu)$ after diagonalizing the atomic and magnetic Hamiltonians presented in Sections 2.1 and 2.2.

3. THE REDISTRIBUTION MATRIX FOR THE COMBINED J AND F STATE INTERFERENCES

The methodology followed to derive the PRD matrix (RM) for the combined case of J and F state interferences in the presence of a magnetic field is similar to that presented in Sowmya et al. (2014b) for F state interference alone. For the sake of clarity, we only present the important equations involved in the derivation.

In a single scattering event, the scattered radiation is related to the incident radiation through the Mueller matrix given by

$$\mathbf{M} = \mathbf{TWT}^{-1}. \quad (6)$$

Here, $\mathbf{T}$ and $\mathbf{T}^{-1}$ are the purely mathematical transformation matrices and $\mathbf{W}$ is the coherency matrix for a transition $a \rightarrow b \rightarrow f$ defined by

$$\mathbf{W} = \sum_a \sum_f \boldsymbol{w} \otimes \boldsymbol{w}^*. \quad (7)$$

Note that the summations over the initial (a) and final (f) states are incoherent, and therefore do not allow the lower levels to interfere. $\boldsymbol{w}$ in the above equation is the Jones matrix and its elements are given by the Kramers–Heisenberg formula, which gives the complex probability amplitudes for the scattering $a \rightarrow b \rightarrow f$ as

$$w_{\alpha\beta} \sim \sum_b \frac{\langle f|\ \mathbf{r}\cdot\mathbf{e}_\alpha\ |b\rangle\langle b|\ \mathbf{r}\cdot\mathbf{e}_\beta\ |a\rangle}{\omega_{bf} - \omega - \mathrm{i}\gamma/2}. \quad (8)$$

Here, $\omega = 2\pi\xi$ is the circular frequency of the scattered radiation. $\hbar\omega_{bf}$ is the energy difference between the excited and final levels and γ is the damping constant.

Using Equation (4) in the Kramers–Heisenberg formula, and noting that $L_f = L_a$ and using the Wigner–Eckart theorem (see Equations (2.96) and (2.108) of LL04), we arrive at

$$\begin{aligned} w_{\alpha\beta} \sim\ & (2L_a+1) \sum_{k_b\mu_b J_a J_f J_b J_{b''} F_a F_f F_b F_{b''}} \\ & \times \sum_{qq''} (-1)^{q-q''}(-1)^{J_f+J_a+J_b+J_{b''}} \\ & \times C^{k_f}_{J_f F_f}\left(L_a SI_s,\ \mu_f\right) C^{k_a}_{J_a F_a}\left(L_a SI_s,\ \mu_a\right) \\ & \times C^{k_b}_{J_b F_b}\left(L_b SI_s,\ \mu_b\right) C^{k_b}_{J_{b''} F_{b''}}\left(L_b SI_s,\ \mu_b\right) \\ & \times \sqrt{(2F_a+1)(2F_f+1)(2F_b+1)(2F_{b''}+1)} \\ & \times \sqrt{(2J_a+1)(2J_f+1)(2J_b+1)(2J_{b''}+1)} \\ & \times \begin{pmatrix} F_b & F_f & 1 \\ -\mu_b & \mu_f & -q \end{pmatrix} \begin{pmatrix} F_{b''} & F_a & 1 \\ -\mu_b & \mu_a & -q'' \end{pmatrix} \\ & \times \begin{Bmatrix} J_f & J_b & 1 \\ F_b & F_f & I_s \end{Bmatrix} \begin{Bmatrix} J_a & J_{b''} & 1 \\ F_{b''} & F_a & I_s \end{Bmatrix} \\ & \times \begin{Bmatrix} L_a & L_b & 1 \\ J_b & J_f & S \end{Bmatrix} \begin{Bmatrix} L_a & L_b & 1 \\ J_{b''} & J_a & S \end{Bmatrix} \\ & \times \varepsilon^{\alpha *}_q \varepsilon^{\beta}_{q''}\ \Phi_\gamma\left(\nu_{k_b\mu_b k_f\mu_f} - \xi\right). \end{aligned} \quad (9)$$

Here, ε are the spherical vector components of the polarization unit vectors ($\mathbf{e}_\alpha$ and $\mathbf{e}_\beta$) with α and β referring to the scattered and incident rays, respectively. $\Phi_\gamma(\nu_{k_b\mu_b k_f\mu_f} - \xi)$ is the frequency-normalized profile function defined as

$$\Phi_\gamma\left(\nu_{k_b\mu_b k_f\mu_f} - \xi\right) = \frac{1/\pi\mathrm{i}}{\nu_{k_b\mu_b k_f\mu_f} - \xi - \mathrm{i}\gamma/4\pi}, \quad (10)$$

where we have used an abbreviation

$$\begin{aligned} \nu_{k_b\mu_b k_f\mu_f} &= \nu_{L_b SI_s k_b\mu_b, L_a SI_s k_f\mu_f} \\ &= \nu_{L_b L_a} + \frac{E_{k_b}\left(L_b SI_s,\ \mu_b\right) - E_{k_f}\left(L_a SI_s,\ \mu_f\right)}{h}, \end{aligned} \quad (11)$$

with h being the Planck constant.

Inserting Equation (9) into Equation (7), and after elaborate algebra (see for example Sowmya et al. 2014b), we obtain the normalized RM, $\mathbf{R}^{\mathrm{II}}_{ij}$, for type-II scattering in the laboratory frame as

$$\begin{aligned} \mathbf{R}^{\mathrm{II}}_{ij}(x, \boldsymbol{n}, x', \boldsymbol{n}'; \boldsymbol{B}) =\ & \frac{3(2L_b+1)}{(2S+1)(2I_s+1)} \\ & \times \sum_{KK'Qk_a\mu_a k_f\mu_f k_b\mu_b k_{b'}\mu_{b'} qq'q''q'''} \sum \sum (-1)^{q-q'''+Q} \\ & \times \sqrt{(2K+1)(2K'+1)} \cos\beta_{k_{b'}\mu_{b'}, k_b\mu_b}\, \mathrm{e}^{\mathrm{i}\beta_{k_{b'}\mu_{b'}, k_b\mu_b}} \\ & \times \left[\left(h^{\mathrm{II}}_{k_b\mu_b, k_{b'}\mu_{b'}}\right)_{k_a\mu_a k_f\mu_f} + \mathrm{i}\left(f^{\mathrm{II}}_{k_b\mu_b, k_{b'}\mu_{b'}}\right)_{k_a\mu_a k_f\mu_f}\right] \\ & \times \sum_{J_a J_{a'} J_f J_{f'} J_b J_{b'} J_{b''} J_{b'''} F_a F_{a'} F_f F_{f'} F_b F_{b'} F_{b''} F_{b'''}} \sum \\ & \times C^{k_f}_{J_f F_f}\left(L_a SI_s,\ \mu_f\right) C^{k_a}_{J_a F_a}\left(L_a SI_s,\ \mu_a\right) \\ & \times C^{k_b}_{J_b F_b}\left(L_b SI_s,\ \mu_b\right) C^{k_b}_{J_{b''} F_{b''}}\left(L_b SI_s,\ \mu_b\right) \\ & \times C^{k_f}_{J_{f'} F_{f'}}\left(L_a SI_s,\ \mu_f\right) C^{k_a}_{J_{a'} F_{a'}}\left(L_a SI_s,\ \mu_a\right) \\ & \times C^{k_{b'}}_{J_{b'} F_{b'}}\left(L_b SI_s,\ \mu_{b'}\right) C^{k_{b'}}_{J_{b'''} F_{b'''}}\left(L_b SI_s,\ \mu_{b'}\right) \\ & \times (-1)^{J_a+J_{a'}+J_f+J_{f'}+J_b+J_{b'}+J_{b''}+J_{b'''}} \\ & \times \sqrt{(2J_a+1)(2J_f+1)(2J_{a'}+1)(2J_{f'}+1)} \\ & \times \sqrt{(2J_b+1)(2J_{b'}+1)(2J_{b''}+1)(2J_{b'''}+1)} \\ & \times \sqrt{(2F_a+1)(2F_f+1)(2F_{a'}+1)(2F_{f'}+1)} \\ & \times \sqrt{(2F_b+1)(2F_{b'}+1)(2F_{b''}+1)(2F_{b'''}+1)} \end{aligned}$$

$$\times \begin{pmatrix} F_b & F_f & 1 \\ -\mu_b & \mu_f & -q \end{pmatrix} \begin{pmatrix} F_{b'} & F_{f'} & 1 \\ -\mu_{b'} & \mu_f & -q' \end{pmatrix}$$
$$\times \begin{pmatrix} F_{b''} & F_a & 1 \\ -\mu_b & \mu_a & -q'' \end{pmatrix} \begin{pmatrix} F_{b'''} & F_{a'} & 1 \\ -\mu_{b'} & \mu_a & -q''' \end{pmatrix}$$
$$\times \begin{pmatrix} 1 & 1 & K \\ q & -q' & -Q \end{pmatrix} \begin{pmatrix} 1 & 1 & K' \\ q''' & -q'' & Q \end{pmatrix}$$
$$\times \begin{Bmatrix} J_f & J_b & 1 \\ F_b & F_f & I_s \end{Bmatrix} \begin{Bmatrix} J_{f'} & J_{b'} & 1 \\ F_{b'} & F_{f'} & I_s \end{Bmatrix}$$
$$\times \begin{Bmatrix} J_a & J_{b''} & 1 \\ F_{b''} & F_a & I_s \end{Bmatrix} \begin{Bmatrix} J_{a'} & J_{b'''} & 1 \\ F_{b'''} & F_{a'} & I_s \end{Bmatrix}$$
$$\times \begin{Bmatrix} L_a & L_b & 1 \\ J_b & J_f & S \end{Bmatrix} \begin{Bmatrix} L_a & L_b & 1 \\ J_{b'} & J_{f'} & S \end{Bmatrix}$$
$$\times \begin{Bmatrix} L_a & L_b & 1 \\ J_{b''} & J_a & S \end{Bmatrix} \begin{Bmatrix} L_a & L_b & 1 \\ J_{b'''} & J_{a'} & S \end{Bmatrix}$$
$$\times (-1)^Q \mathcal{T}^K_{-Q}(i, \boldsymbol{n}) \mathcal{T}^{K'}_{Q}(j, \boldsymbol{n}'). \quad (12)$$

Here, $\mathcal{T}^K_Q(i, \boldsymbol{n})$ are the irreducible spherical tensors for polarimetry (Landi Degl'Innocenti 1984) with $i = 0, 1, 2, 3$ referring to the Stokes parameters, the multipolar index $K = 0, 1, 2$, and $Q \in [-K, K]$. $\boldsymbol{n}'$ and $\boldsymbol{n}$ represent the directions of the incident and scattered rays, respectively, and $\boldsymbol{B}$ is the vector magnetic field. x' and x are the non-dimensional frequencies in Doppler width units (see Appendix A). $\beta_{k_{b'}\mu_{b'}k_b\mu_b}$ is the Hanle angle given by

$$\tan \beta_{k_{b'}\mu_{b'}k_b\mu_b} = \frac{\nu_{k_{b'}\mu_{b'}k_a\mu_a} - \nu_{k_b\mu_b k_a\mu_a}}{\gamma/2\pi}. \quad (13)$$

The explicit forms of the auxiliary functions $h^{\rm II}$ and $f^{\rm II}$ appearing in Equation (12) are given in Appendix A. When $I_s = 0$, Equation (12) reduces to the PRD matrix for J state interference alone (see Equation (11) of Sowmya et al. 2014a). When FS is neglected, Equation (12) reduces to the expression of RM for pure F state interference (see Equation (16) of Sowmya et al. 2014b). When we neglect both FS and HFS, we recover RM for the $L_a \rightarrow L_b \rightarrow L_a$ transition (analogous to a two-level atom case) in the presence of a magnetic field.

4. RESULTS

In this section, we present the results obtained from the combined theory for the case of the single scattering of an unpolarized, spectrally flat incident radiation beam by an atom with both non-zero electron and nuclear spins. Considering the relevance to solar applications, we choose the D line system at 6708 Å from neutral ^{6}Li and ^{7}Li isotopes as an example to test the formalism developed. We take the values of the atomic parameters and isotope abundances for this system from Table 1 of Belluzzi et al. (2009).

4.1. Level-crossings and Avoided Crossings

In Figures 2 and 3, we show the dependence of the energies of the levels in the ^{2}P terms of the ^{6}Li and ^{7}Li isotopes on the magnetic field strength. Such figures provide us with information on the field strength regimes in which processes like the Zeeman effect, incomplete PB effect, and complete PB effect operate. They help us to choose the magnetic field strength values for studying the effects of level-crossing on the Stokes profiles. We choose different scales for the x-axes in different panels to bring out the level-crossings which occur at different field strengths due to the difference in the magnitudes of FS and HFS. The y-axes in all of the panels in both figures denote the energy shift of the levels from the parent $L = 1$ level.

In panels (a) and (c) of Figure 2, we plot the energies of the magnetic substates of the F states belonging to the $^2P_{3/2}$ and $^2P_{1/2}$ levels of ^{6}Li, respectively, as a function of the field strength. Since the nuclear spin of ^{6}Li is 1, we have half-integer values for F. In these panels, we see that the magnetic substates of the F states of $^2P_{3/2}$ cross at nine points while those of $^2P_{1/2}$ do not cross. We note a similar behavior in the case of the F states belonging to the $^2P_{3/2}$ and $^2P_{1/2}$ levels of ^{7}Li (see panels (b) and (d), respectively). The magnetic substates of the F states of $^2P_{1/2}$ do not cross while those of $^2P_{3/2}$ cross at 14 points. In the weak field regime (e.g., 0–60 G), we see the PB effect for the F states, and in the strong field regime (for kG fields) we see the PB effect for the J states. In Tables 1 and 2, we list the quantum numbers of the levels which cross along with their corresponding field strengths for the weak field regime. The numbers indicated in boldface in these tables correspond to those crossings which satisfy $\Delta\mu = \mu_{b'} - \mu_b = \pm 2$. We discuss the effects of these level-crossings on the polarization in later sections.

In panels (a) and (d) of Figure 3, we plot the energies of the magnetic substates of the ^{2}P terms of ^{6}Li and ^{7}Li as a function of the magnetic field strength. In these panels, the points where the levels cross are denoted as c1 and c2 for ^{6}Li and as c′1 and c′2 for ^{7}Li. When we zoom into these crossing points, we see other interesting phenomena (see panels (b), (c), (e), and (f)). For example, at c1, we see a crossing of the bunch of lowermost three levels going downward in Figure 2(a) with the three levels going upward in Figure 2(c). Although the magnetic substates of the F states appear to be degenerate in Figure 3(a), they are not fully degenerate, as can be seen in Figure 3(b). Similar behavior can be seen in Figures 3(c), (e), and (f), and the levels correspond to the magnetic substates of the F states shown in Figure 2.

In addition to the usual level-crossings, we see several avoided crossings in Figures 3(b), (c), (e), and (f). For example, in panel (b), we see one avoided crossing marked a1, two in panel (c) marked a2 and a3, two in panel (e) marked a′1 and a′2, and three in panel (f) marked a′3, a′4, and a′5. As we can see from the figure, these avoided crossings take place between the magnetic substates with the same μ values ($-1/2$ in panel (b), $-3/2$ and $-1/2$ in panel (c), 0 and -1 in panel (e), and -2, -1, and 0 in panel (f)). The levels with the same μ cannot cross due to the small interaction that takes place between them. This interaction is determined by the off-diagonal elements of the magnetic hyperfine interaction Hamiltonian which couple the states with different J values (Brog et al. 1967; Wieder & Eck 1967; Arimondo et al. 1977). A rapid transformation in the eigenvector basis takes place around the region of avoided crossing. This is described in Bommier (1980) and in LL04 (see also Sowmya et al. 2014a, 2014b).

4.2. Line Splitting Diagrams

The line splitting diagram shows the displacement of the magnetic components from the line center (corresponding to the wavelength of the $L = 0 \rightarrow 1 \rightarrow 0$ transition in the

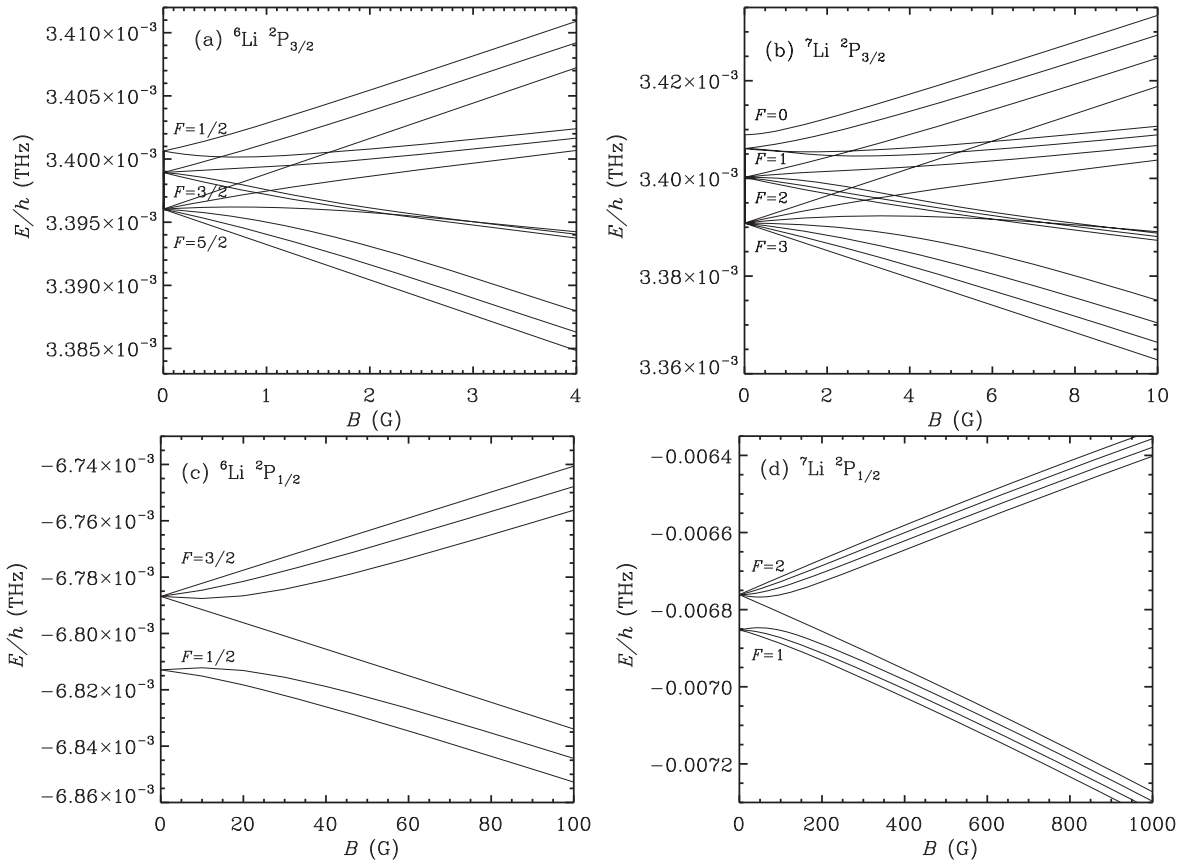

Figure 2. Energies of the HFS magnetic substates as a function of the magnetic field strength for ^{6}Li (left column) and ^{7}Li (right column). Panels (a) and (b) correspond, respectively, to the $^2P_{3/2}$ levels of ^{6}Li and ^{7}Li, while panels (c) and (d) correspond to the $^2P_{1/2}$ levels of ^{6}Li and ^{7}Li, respectively. The nuclear spins of ^{6}Li and ^{7}Li are 1 and 3/2, respectively.

reference isotope ^{7}Li) and the strengths of these components for a given field strength. In Figure 4, we show the line splitting diagrams for different B values. We take into account the isotope shift and the solar abundances of the two isotopes while computing the strengths and magnetic shifts. As mentioned earlier, the components arising for $B = 0$ correspond to the transitions between the unperturbed F states. We see that the hyperfine structure components of the D lines are well separated when $B = 0$ due to the relatively large FS. When the magnetic field is applied, the degeneracy of the magnetic substates is lifted. As a result, 70 allowed transitions take place in ^{6}Li and 106 in ^{7}Li. This explains why the diagrams become crowded as the field strength increases. We see that the magnetic displacements increase with an increase in B as expected. In the diagrams shown, we note that the MS is nonlinear and is a characteristic of the incomplete PB regime.

4.3. Single Scattered Stokes Profiles

In this section, we present the Stokes profiles for various B values computed using the combined theory for the single scattering case. We choose a coordinate system (see Figure 5) in which the magnetic field lies in the horizontal (xy) plane making angles $\theta_B = 90°$ and $\chi_B = 45°$. We make this choice following Stenflo (1998) in order to bring out clearly the effects of the magnetic field. We assume the unpolarized incident ray to be along the vertical (z-axis) and the scattered ray (or the line of sight) to lie in the horizontal plane along the x-axis. Thus, the angles for the incident and the scattered rays become $\mu' = 1$, $\chi' = 0°$, $\mu = 0$, and $\chi = 0°$. We use the fact that the lithium lines are optically thin and only single scattering is considered here to add the Stokes profiles computed for the individual isotopes after weighting them by their respective abundances. In Figures 6–9, we compare the single scattered Stokes profiles for three cases: the cases of pure F state interference (dotted lines) represented by a two-level atom with hyperfine structure, pure J state interference (dashed lines) represented by a two-term atom without hyperfine structure, and the combined theory (solid lines) represented by a two-term atom with hyperfine structure. We choose a Doppler width of 60 mÅ for all of the components of the multiplet when computing the Stokes profiles. For this particular value of the Doppler width, the theoretical Q/I profile closely resembles the observed Q/I profile (see Belluzzi et al. 2009). We use the Einstein A coefficient of $3.689 \times 10^7\ s^{-1}$ for all of the components.

In Figure 6, we show the Stokes profiles computed in the absence of magnetic fields for 100% ^{7}Li in panel (a), for 100% ^{6}Li in panel (b), and for both the isotopes combined according to their percentage abundance in panel (c). In panels (a) and (b), we see two peaks corresponding to the D lines of the two isotopes in intensity. The intensities of the D lines in both the isotopes are of similar magnitude since we have assumed 100% abundance for the two isotopes. We also note that the wavelength positions of the D lines of ^{6}Li are different from those of ^{7}Li due to the isotope shift. In panel (c), we see two distinct peaks in intensity. The first peak to the left is due to the ^{7}Li D_2 line. The second peak falls at the line center positions of

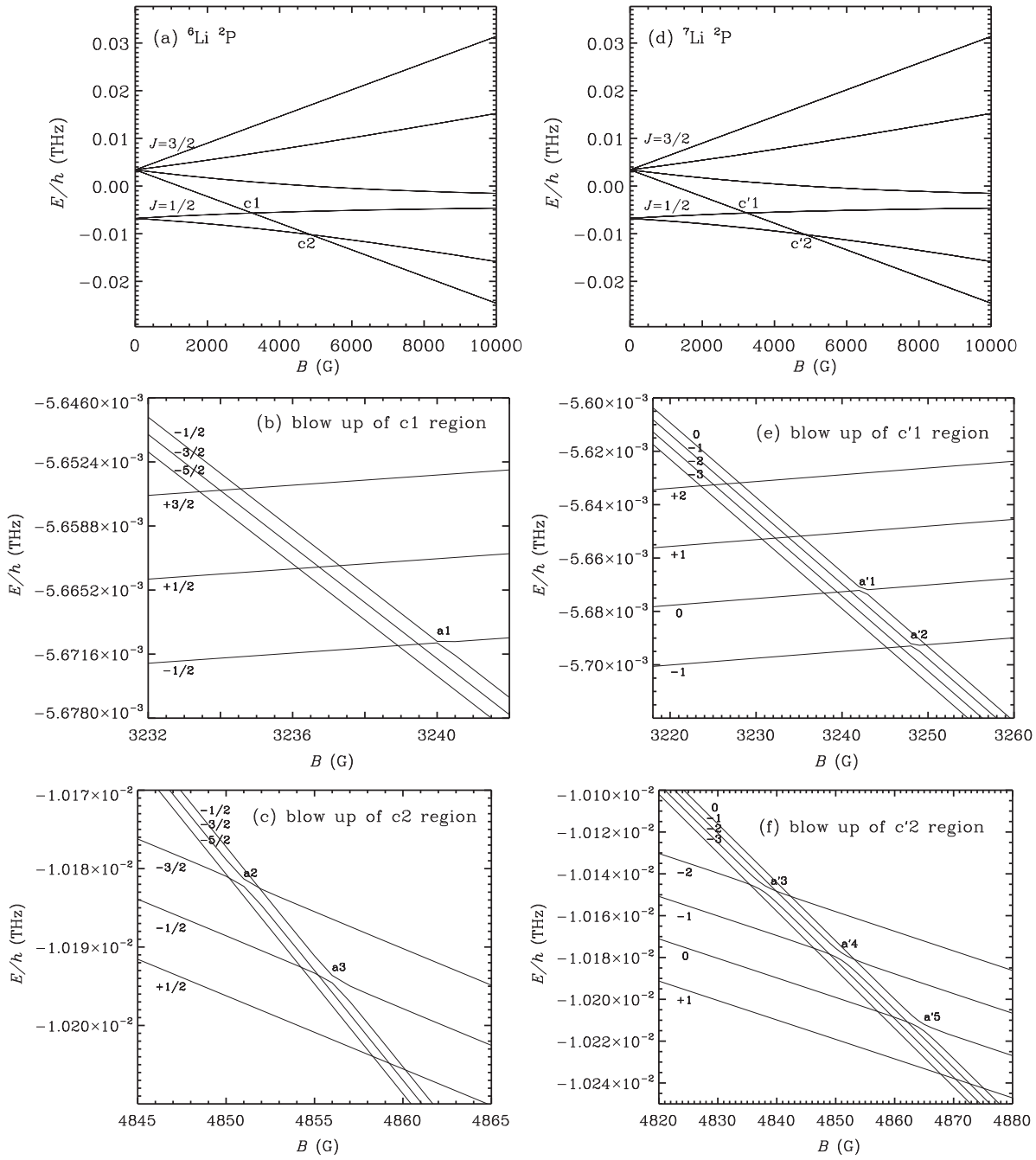

Figure 3. Energies of the magnetic substates belonging to the ^{2}P terms as a function of the magnetic field strength for ^{6}Li (a) and ^{7}Li (d). Blow up of the crossing regions c1 (b) and c2 (c) in ^{6}Li and c′1 (e) and c′2 (f) in ^{7}Li. In the panels (b), (c), (e), and (f) the levels are identified by their magnetic quantum number values μ.

Table 1
Magnetic Field Strengths (Approximate Values in G) for Which the Magnetic Substates of the F States Cross in the ^{6}Li Isotope

$F_b \backslash F_{b'}$		1/2	3/2	3/2	3/2
	$\mu_b \backslash \mu_{b'}$	1/2	−1/2	1/2	3/2
3/2	−3/2	**0.57**	…	…	…
5/2	−5/2	1.61	**1.26**	0.72	0.63
5/2	−3/2	…	…	**1.3**	0.9
5/2	−1/2	…	…	2.93	**2.25**

Note. For instance, the crossing between ($\mu_b = -3/2$, $F_b = 3/2$) and ($\mu_{b'} = 1/2$, $F_{b'} = 1/2$) occurs at $B \sim 0.57$ G. The numbers highlighted in boldface represent the field strength values for which the level-crossings corresponding to $\Delta\mu = \mu_{b'} - \mu_b = \pm 2$ occur.

Table 2
Magnetic Field Strengths (Approximate Values in G) for Which the Magnetic Substates of the F States Cross in the ^{7}Li Isotope

$F_b \backslash F_{b'}$		1	1	2	2	2	2
	$\mu_b \backslash \mu_{b'}$	0	+1	−1	0	+1	+2
2	−2	**2.2**	2.6	…	…	…	…
3	−3	5.2	5.95	**4.15**	2.65	2.35	2.1
3	−2	…	…	…	**3.7**	3.25	2.95
3	−1	…	…	…	8.8	**7.25**	6.0

Note. For instance, the crossing between ($\mu_b = -2$, $F_b = 2$) and ($\mu_{b'} = 0$, $F_{b'} = 1$) occurs at $B \sim 2.2$ G. The numbers highlighted in boldface represent the field strength values for which the level-crossings corresponding to $\Delta\mu = \mu_{b'} - \mu_b = \pm 2$ occur.

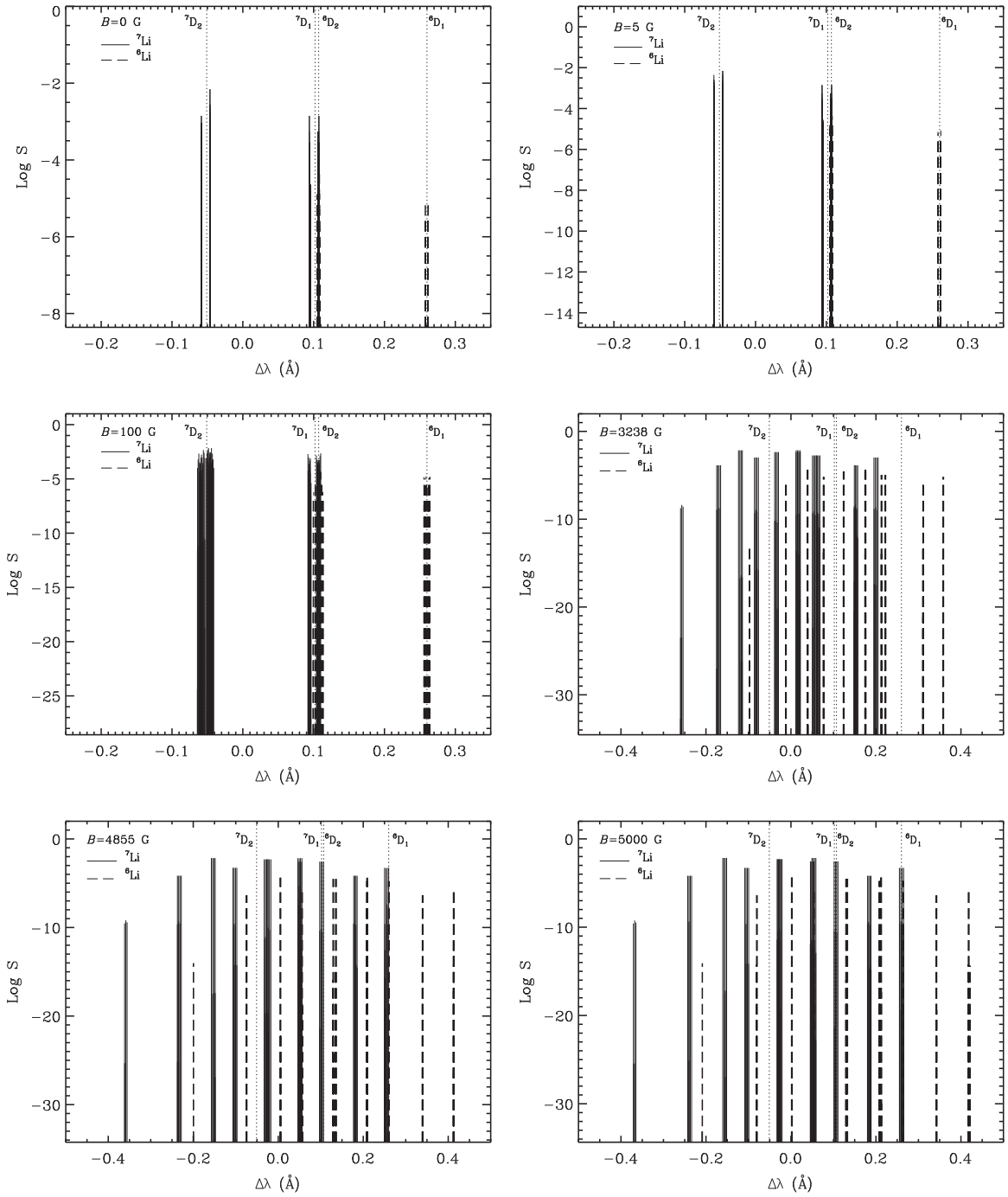

Figure 4. Line splitting diagrams for the two lithium isotopes for the field strengths indicated. The solid lines represent the magnetic components of ^{7}Li while the dashed lines represent those of ^{6}Li. Vertical dotted lines mark the positions of the D lines of the two isotopes. $\Delta\lambda = 0$ corresponds to the line center wavelength of $L = 0 \rightarrow 1 \rightarrow 0$ transition in ^{7}Li.

^{7}Li D_1 and ^{6}Li D_2. However, the dominant contribution comes from ^{7}Li D_1 due to its relatively larger abundance. A small bump to the right of the second peak is due to the ^{6}Li D_1 line. A small difference in the intensity at the ^{7}Li D_2 peak between the dashed lines and the other two cases is seen in panels (a) and (c). It is clear from the figure that this discrepancy is caused by ^{7}Li. Comparing the solid, dotted, and dashed profiles, we come to the conclusion that the HFS is at the origin of this discrepancy. This is because the solid and dotted lines computed by including HFS perfectly match and only the dashed lines computed without HFS differ from the other two cases. The discrepancy is very small in the case of ^{6}Li because of smaller HFS in ^{6}Li compared to that in ^{7}Li. The reason for this discrepancy is due to the asymmetric splitting of the HFS components about the given J state and also due to the finite widths of the components. This difference decreases (graphically indistinguishable) when a magnetic field is applied (for example, when $B = 5$ G as seen in Figure 7) because of the superposition of a large number of magnetic components. In contrast, this difference is about an order of magnitude larger in

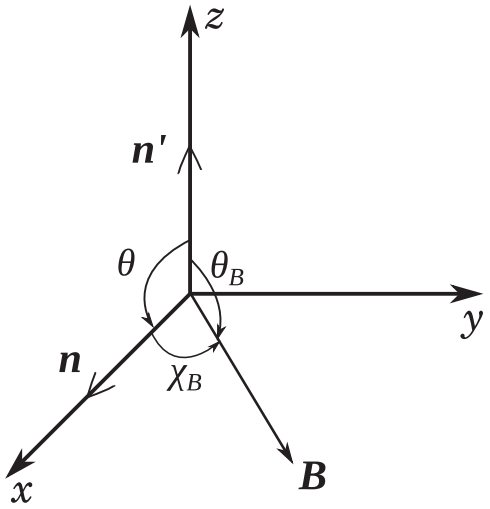

Figure 5. Scattering geometry considered for the results presented in Section 4.3.

the non-magnetic case. As we increase the field strength, the intensity profiles broaden due to an increased separation between the magnetic components.

When $B = 0$, the Q/I profiles exhibit a multi-step behavior around the line center positions of the D_1 and D_2 lines of both isotopes. We see the effects of quantum interference clearly in Q/I. In the ^{7}Li D_2 core, significant depolarization is caused by the HFS compared to the case where this splitting is neglected (compare the solid and dashed lines in panels (a) and (c)). A similar depolarization is also exhibited by the core of the ^{6}Li D_2 line (see panels (b) and (c)). However, in the scale adopted, the solid and dashed lines appear to merge around the core of ^{6}Li D_2 in panel (c), as the Q/I values of ^{6}Li D_2 are an order of magnitude smaller than those of ^{7}Li D_2 because of their relative abundances. The D_1 lines remain upolarized. As expected, the solid lines merge with the dotted line in the cores of lithium lines while they coincide with the dashed lines in the wings. When a magnetic field is applied, we see a depolarization in Q/I and a generation of the U/I signal in the cores of the lithium lines due to the Hanle effect. We note that the combined theory results match more closely the pure J state interference results for fields of the order of 100 G. This behavior continues until the level-crossing field strength of $B = 3238$ G for fine structure is reached.

For kG fields, we are by far in the complete PB regime for the F states. In this regime, the J and I_s couple strongly to the magnetic field and the interaction between J and I_s becomes negligible. Therefore, one would expect the HFS magnetic substates to be fully degenerate, and therefore the solid and dashed lines should match closely for fields of the order of kG. However, for the level-crossing field strengths, we see considerable differences between the solid and dashed lines, especially in U/I. In order to understand this, we compare the Stokes profiles for ^{7}Li and ^{6}Li separately in panel (a) and (b) of Figure 8 with the combined profiles in panel (c). We do this to check whether a particular isotope is giving rise to this difference. We note that this difference between the solid and dashed lines prevails in all three panels (i.e., in both isotopes). We attribute this difference in the shape and amplitude between the solid and the dashed lines to HFS, the level-crossings, and avoided crossings between the HFS magnetic substates. When

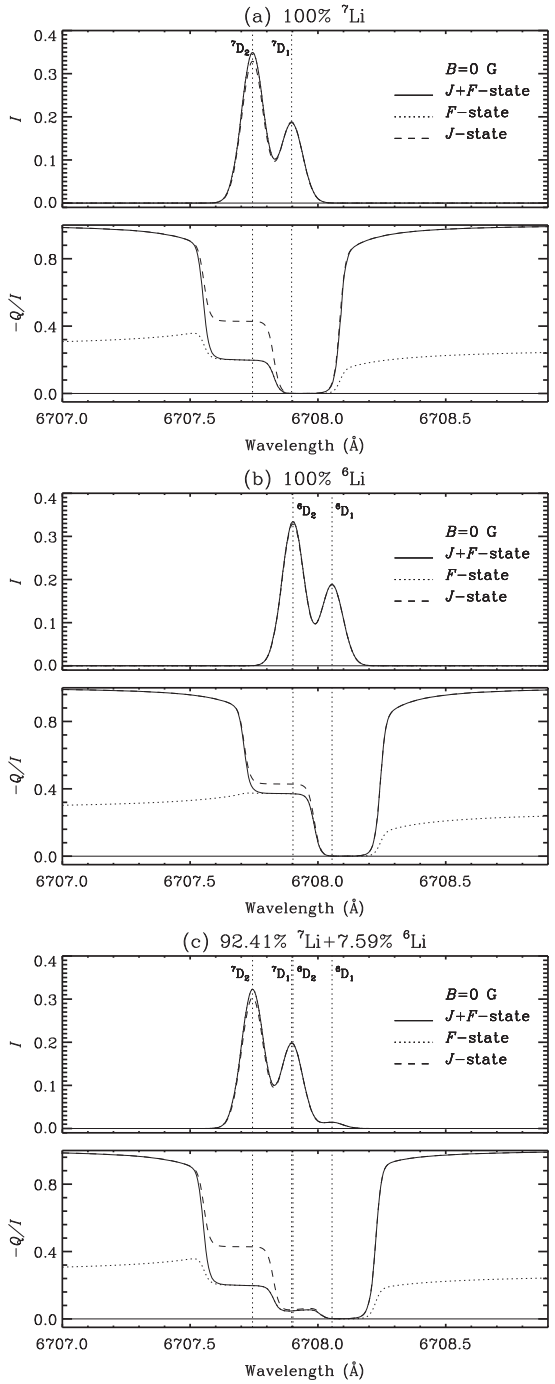

Figure 6. Single scattered Stokes profiles for the lithium D line system in the absence of a magnetic field: (a) 100% ^{7}Li, (b) 100% ^{6}Li, and (c) ^{7}Li and ^{6}Li combined according to their percentage abundance. The line types are indicated in the intensity panels. The geometry considered for scattering is $\mu = 0$, $\mu' = 1$, $\chi = 0°$, and $\chi' = 0°$. The vertical dotted lines represent the line center wavelength positions of the ^{7}Li D_2, ^{7}Li D_1, ^{6}Li D_2, and ^{6}Li D_1 lines in the absence of magnetic fields.

we look at Figure 3, we find that the HFS magnetic substates have finite energy differences and are not fully degenerate in the complete PB regime for the F states. We see several crossings as well as a few avoided crossings. These level-crossings and avoided crossings between the non-degenerate HFS magnetic substates lead to a modification of the coherence and significant Hanle rotation, thereby affecting the shape and

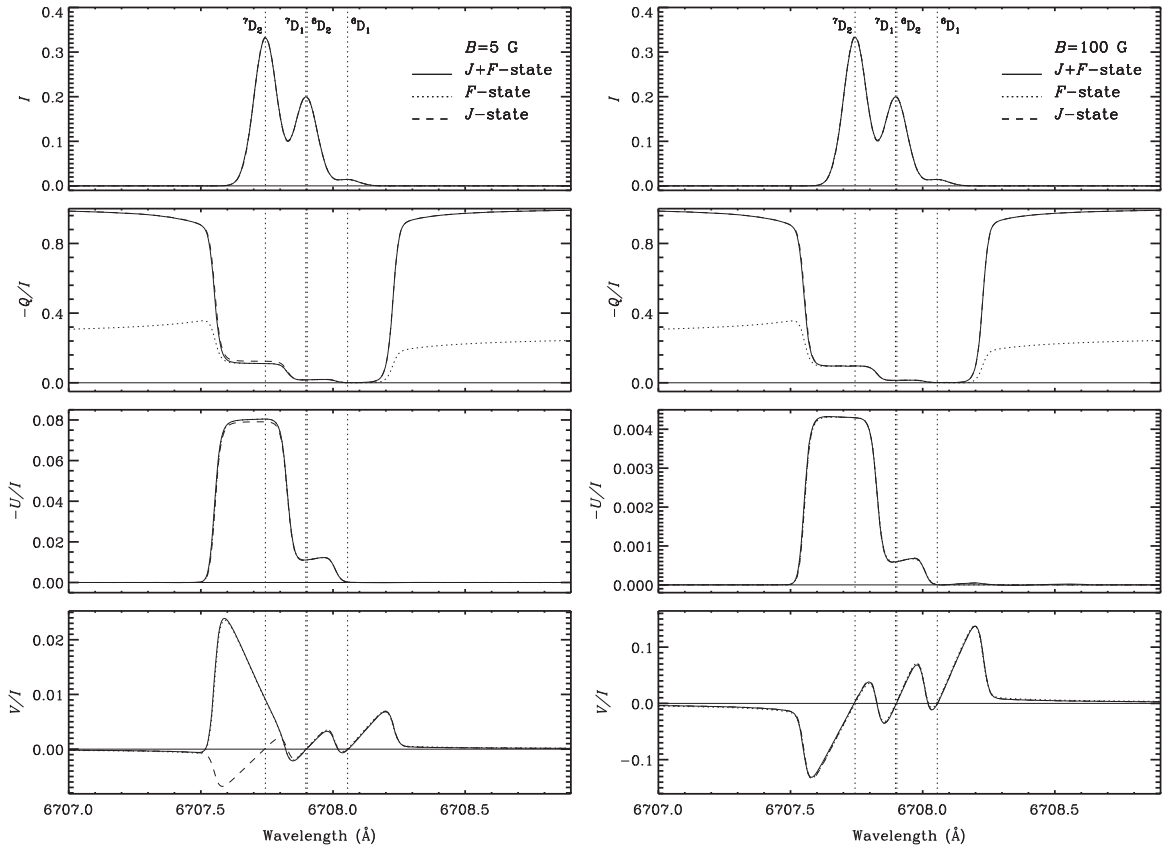

Figure 7. Same as Figure 6, but in the presence of a magnetic field. The left and the right panels correspond to different field strength values. The field orientation ($\theta_B = 90°$, $\chi_B = 45°$) is the same in both the panels. Refer to Section 4.3 for the scattering geometry.

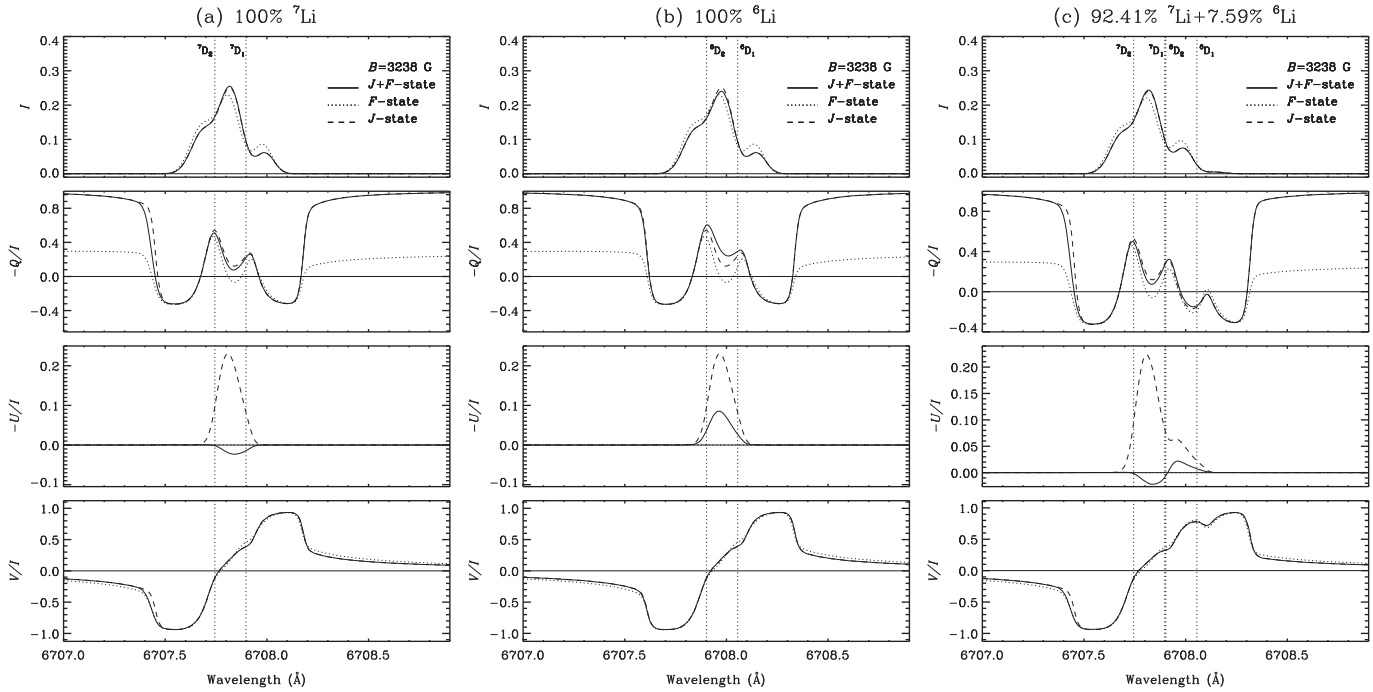

Figure 8. Stokes profiles obtained for $B = 3238$ G: (a) 100% ^{7}Li, (b) 100% ^{6}Li, and (c) ^{7}Li and ^{6}Li combined according to their percentage abundance. Refer to Section 4.3 for the scattering geometry. When $B = 3238$ G, the U/I values are so small for the dotted line case that they become indistinguishable from the zero line.

amplitude of the U/I profiles. The HFS effects show more prominently in the polarization diagrams which will be discussed in Section 4.5. For the geometry under consideration, this effect is significantly seen for $B = 3238$ G. For a level-crossing field strength of 4855 G, the Stokes profiles show somewhat different behavior.

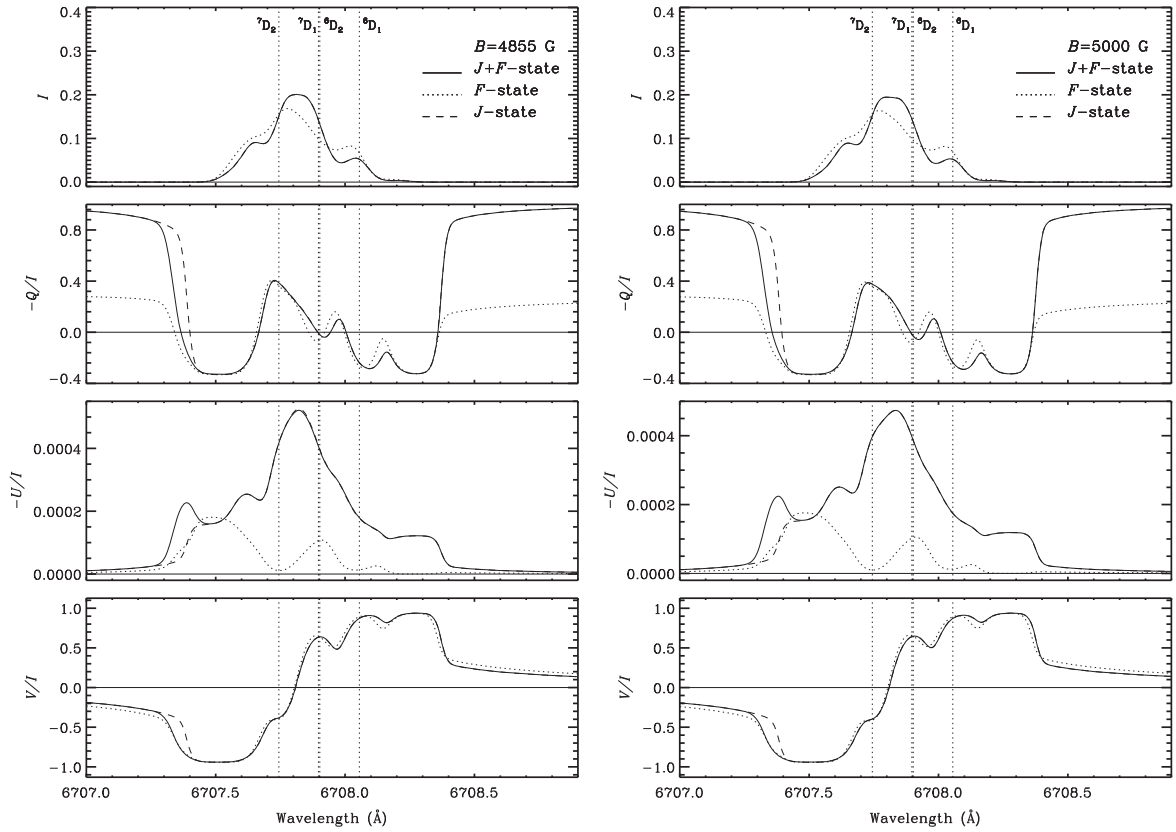

Figure 9. Stokes profiles obtained for $B = 4855$ G and $B = 5000$ G. Refer to Section 4.3 for the scattering geometry.

We also note that for fields of the order of kG, differences between the solid and dashed lines remain only in the far left wing (see Figures 8 and 9). From Figure 8 it is clear that this difference in the far blue wings is only due to the ^{7}Li isotope (compare panels (a)–(c)). This can be understood with the help of the line splitting diagrams for level-crossing fields in Figure 4 in comparison with the corresponding diagrams in Figure 3 of Sowmya et al. (2014a; a direct comparison of the displacements can be made as the zero points in the two figures are the same). In a two-term atom without HFS, when a magnetic field is applied, the various FS magnetic components are either blue or redshifted from the line center depending on their energies. When HFS is included, the HFS magnetic components are distributed around the positions of the FS magnetic components in the absence of HFS. We find that the positions of the HFS magnetic components in Figure 4 correspond well with the wavelength positions of the FS magnetic components in Figure 3 of Sowmya et al. (2014a), except for the bunch of magnetic components to the extreme left represented by solid lines. The magnetic field leads to a large blue shift of this bunch, which consists of three σ_b ($\Delta\mu = \mu_b - \mu_a = +1$), two π ($\Delta\mu = 0$) and one σ_r ($\Delta\mu = -1$) components. These components (otherwise not present at this wavelength position when HFS is neglected) give rise to the systematic difference in Q/I, U/I, and V/I in the far blue wing of the D_2 line of ^{7}Li. However, they do not affect the intensity.

The V/I profiles remain somewhat indistinguishable between the three cases considered, except for very weak fields like 5 G as in Figure 7. F state interference significantly changes the V/I profile at the ^{7}Li D_2 wavelength position. This is a signature of the alignment-to-orientation (A-O) conversion mechanism (see Landi Degl'Innocenti 1982, and LL04) acting in the incomplete PB regime for the F states. As described in LL04, this occurs because of the double summation over K and K' appearing in Equation (12) and because the spherical tensor $\mathcal{T}^K_Q(3, \boldsymbol{n})$ is non-zero only when $K = 1$ (see Equation (33) of Appendix C). This means that circular polarization can be generated by resonance scattering even if the atom is not exposed to circularly polarized light. The alignment present in the radiation field is converted to the orientation in the upper term. This orientation in the upper F states gives rise to circularly polarized light. As discussed earlier, small differences appear in the far blue wings for fields equal to or larger than the level-crossing field strengths.

Finally, we remark that the discussion presented above concerning the comparison of the single scattered Stokes profiles between the three cases (namely, the pure J state, pure F state, and combined J and F interference) also remains valid for other scattering geometries.

In Figure 10, we show the Stokes profiles obtained after including a weakly polarized background continuum. We refer the reader to Section 4.3 of Sowmya et al. (2014a) for details on how we add the continuum contribution and on the parameters used for the continuum. We compare this figure with Figure 4 of Sowmya et al. (2014a) and find that the HFS does not cause any change in the intensities. When $B = 0$ the HFS causes a depolarization in the core of Q/I without affecting the shape of the profile. For other field strengths, there is only a slight difference in the amplitude of the profiles as compared to the case without HFS, although their shapes remain the same. The U/I profiles differ both in amplitude and

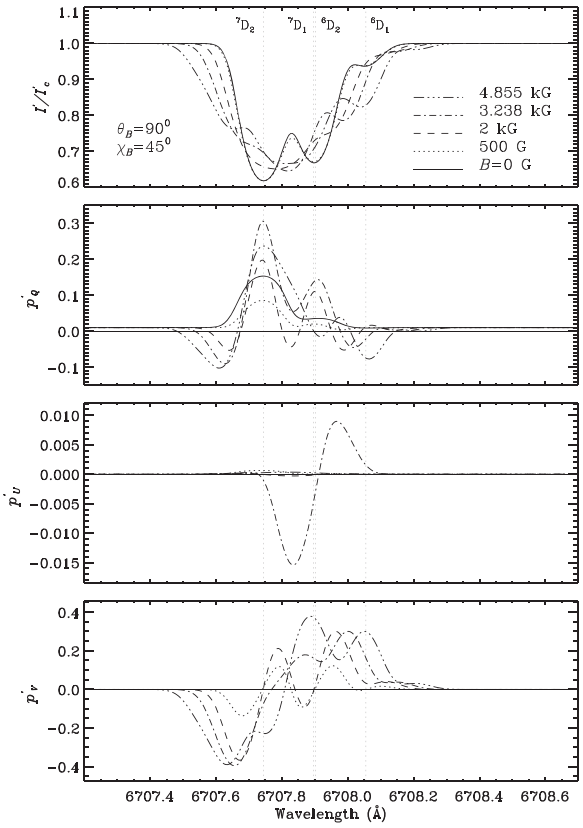

Figure 10. Stokes profiles obtained by including the contribution from the continuum for different values of B. Refer to Section 4.3 for the scattering geometry. The vertical dotted lines represent the positions of the D lines.

shape for $B = 3238$ G. This difference is due to HFS. When HFS is neglected, there is only one level-crossing at this field strength. On the other hand, when HFS is included, there are several level-crossings around this field strength (see Figures 3(b) and (e)). V/I profiles have the same shapes and amplitudes as compared to the case without hyperfine structure.

4.4. Net Circular Polarization (NCP)

In this section, we present the plots of NCP defined as $\int V d\lambda$ as a function of the magnetic field strength B. Since the PB effect causes nonlinear splitting of the magnetic components with respect to the line center, the Stokes V profiles become asymmetric. As a result of this asymmetry, the integration of the Stokes V over the full line profile yields a non-zero value. In the linear Zeeman and complete PB regimes, the V profiles show perfect antisymmetry which causes the NCP to become zero. The A-O conversion mechanism discussed in Section 4.3 further enhances the asymmetry in Stokes V profiles already caused by nonlinear MS, and thereby contributes to the NCP. This mechanism is particularly efficient when the level-crossings satisfy $\Delta\mu = \mu_{b'} - \mu_b = 1$.

In Figure 11, we show the behavior of NCP in different field strength ranges for the scattering geometry: $\mu' = 0$, $\chi' = 0°$, $\mu = 1$, $\chi = 90°$, $\theta_B = 0°$, and $\chi_B = 0°$. This choice of field geometry is made in order to obtain larger values for Stokes V. In panel (a), we show the weak field behavior of NCP. We attribute the non-zero NCP in this regime to the PB effect in the F states and the A-O conversion mechanism taking place in the incomplete PB regime for the F states. We find that the NCP

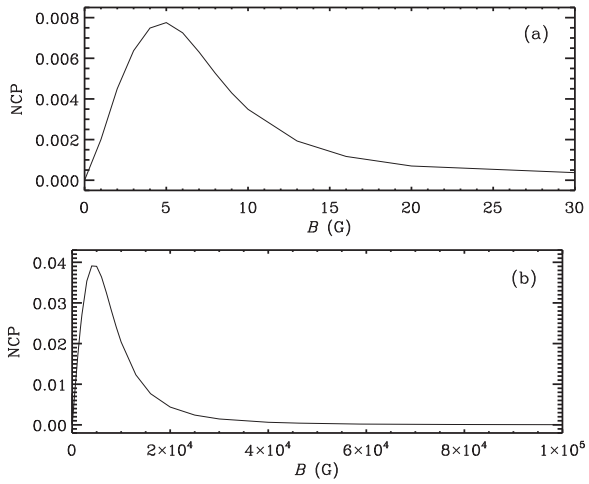

Figure 11. Net circular polarization as a function of the magnetic field strength B. The scattering geometry is characterized by $\mu' = 0$, $\chi' = 0°$, $\mu = 1$, $\chi = 90°$, $\theta_B = 0°$, and $\chi_B = 0°$.

increases with increasing field strength, peaking around the level-crossing field strength (see Tables 1 and 2), and decreases with further increase in B. For fields of the order of kG we see a second peak in NCP whose magnitude is larger than the first peak by an order. This is due to the PB effect in the J states and the A-O conversion mechanism occurring in the incomplete PB regime for the J states. With a further increase in the field strength, we enter the complete PB regime for the J states where the NCP becomes zero.

Detailed discussions on the various mechanisms producing NCP are presented in LL04.

4.5. Polarization Diagrams

In Figure 12, we present the plots of Stokes Q/I versus Stokes U/I (polarization diagrams) for a given B and θ_B and for the full range of χ_B. Refer to the figure caption for the incident and scattered ray directions. θ_B takes values 0°, 70°, 90°, and 110°. We find that the $\theta_B = 70°$ and 110° curves perfectly coincide in all four panels. They take same values for Q/I and U/I at $\chi_B = 0°$ and $\chi_B = 180°$. However, we see that the dependence on χ_B of the $\theta_B = 70°$ curve is somewhat different from that of the $\theta_B = 110°$ curve. By this, we mean that for the $\theta_B = 70°$ case, the Q/I value changes in an anti-clockwise direction from the $\chi_B = 0°$ point while it changes in a clockwise direction from the $\chi_B = 0°$ point for the $\theta_B = 110°$ case. The Q/I value increases with increasing χ_B, reaches a maximum and then decreases till $\chi_B = 180°$. U/I makes a gradual transition from being positive to negative. Q/I again increases with an increase in χ_B and at $\chi_B = 360°$ it resumes the same value it had at $\chi_B = 0°$. U/I now makes a transition from being negative to positive. When $\theta_B = 0°$ the magnetic field is along the z-axis and exhibits azimuthal symmetry. Hence, $\theta_B = 0°$ is just a point in the polarization diagram. For $\theta_B = 90°$ the diagram is symmetric with respect to the $U/I = 0$ line.

In Figure 13, we compare the polarization diagrams obtained at different wavelength points by varying the field strength B for a two-term atom without HFS (dashed curves) and a two-term atom with HFS (solid curves). The geometry considered is described in the caption to the figure. In panel (a), we see a decrease in Q/I with increasing field strength due to the Hanle

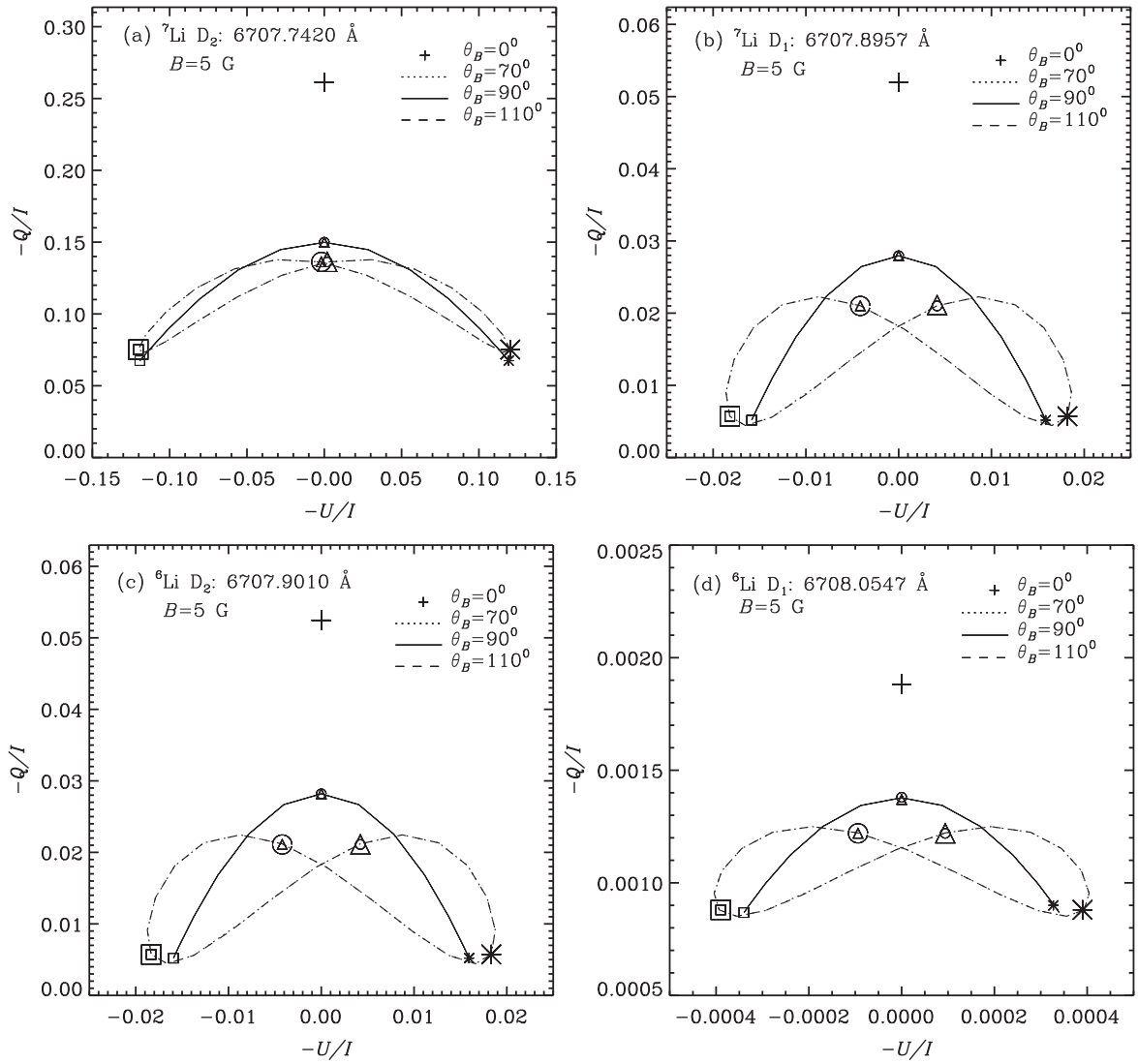

Figure 12. Polarization diagrams obtained at the D line positions for $B = 5$ G and different θ_B as indicated in the panels. The azimuth χ_B of the magnetic field is varied from 0° to 360°. The symbols on the curves mark the χ_B values: *—0°, ∘—70°, □—180°, and △—270°. Since the curves for $\theta_B = 70°$ and 110° coincide, we use symbols that are bigger in size for the $\theta_B = 110°$ case to distinguish it from the $\theta_B = 70°$ curve. The geometry considered is $\mu = 0$, $\mu' = 1$, $\chi = 0°$, and $\chi' = 0°$.

effect. For fields greater than 100 G, we enter the Hanle saturation regime. Q/I starts to increase as we approach the level-crossing field strength (around 3 kG). Loops (i.e., a single circular loop for the dashed line and multiple small loops for the solid line) arise due to several level-crossings (see Figure 3) where the coherence increases and Q/I tends to approach its non-magnetic value. Comparing the solid and dashed curves in Figure 13, the effects of HFS can be clearly seen. First, due to the depolarization caused by HFS, the polarization diagram shrinks in size. Second, multiple small loops are formed (see the solid lines in Figure 13). These multiple loops arise due to several level-crossings that occur only when HFS is included (see Figures 3(b), (c), (e), and (f)). For field strengths larger than the level-crossing field strengths, the Q/I value decreases again and becomes zero around 10 kG. We see the effects due to Rayleigh scattering in strong magnetic fields when we increase the field strength beyond 10 kG (similar to Figure 6(b) of Sowmya et al. 2014a). In panel (b), we show the polarization diagram computed at the ^{6}Li D$_2$ wavelength position. Since the ^{7}Li D$_1$ position nearly coincides with that of ^{6}Li D$_2$, we see the combined effect of both lines. However, due to the large abundance of ^{7}Li, the behavior of the polarization diagram is dominated by the contribution from ^{7}Li D$_1$. Since ^{7}Li D$_1$ is unpolarized, the small arcs seen for weak fields are due to the ^{6}Li D$_2$ line. After the Hanle saturation field strength (30 G), the polarization diagrams essentially show behavior similar to the corresponding polarization diagrams in panel (a). In panel (c), we show the polarization diagram for the ^{6}Li D$_1$ position. The D$_1$ line remains unpolarized till the level-crossing field strength (around 3 kG) is reached. Around the level-crossing field strength, we see a bigger loop for the case without HFS (dashed line) and a smaller loop for the case with HFS (solid line).

5. CONCLUSIONS

We present a formalism to treat the combined interferences between the magnetic substates of the hyperfine structure states pertaining to different fine structure states of the same term including the effects of PRD in scattering. Using the Kramers–Heisenberg approach, we calculate the polarized scattering cross section (i.e., the redistribution matrix) for this process. We also demonstrate the behavior of the redistribution matrix

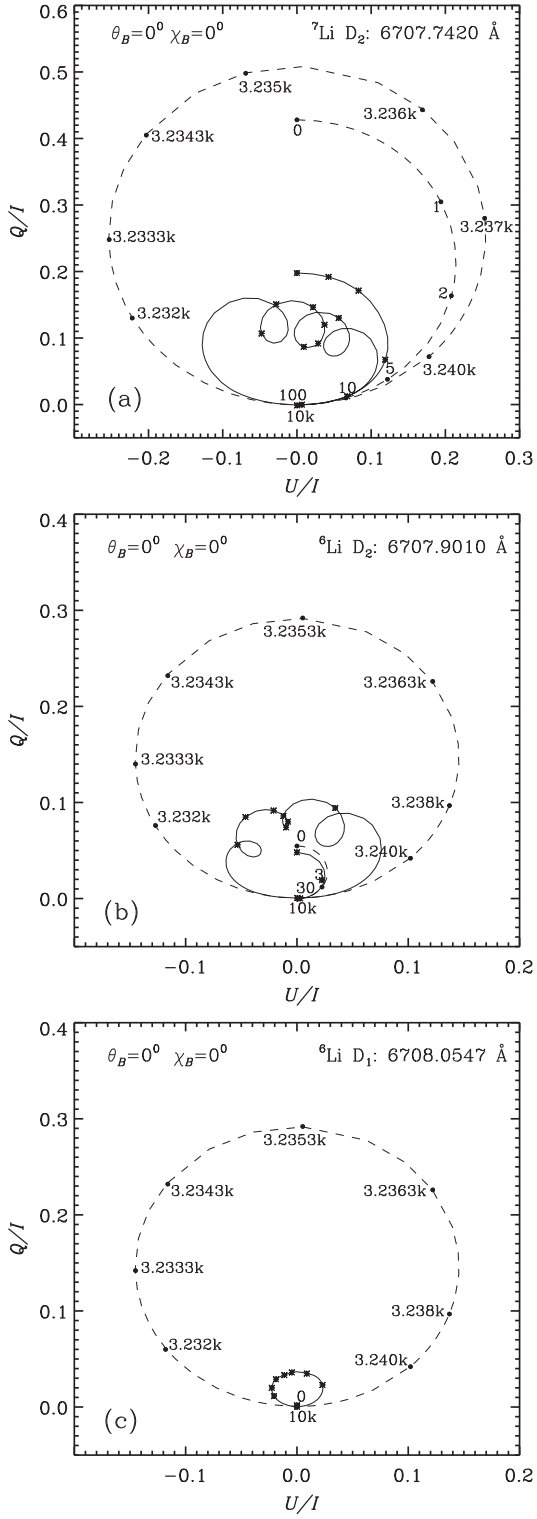

Figure 13. Polarization diagrams obtained at the D line positions for a given orientation of the magnetic field. The dashed lines correspond to the pure J state interference case without HFS while the solid lines correspond to the combined theory case (including HFS). The magnetic field strength values are marked along the dashed curves in Gauss, with "k" meaning a factor of 1000. The asterisks on the solid curves represent the same field strength values as indicated for the dashed curves. The scattering geometry considered is $\mu = 1$, $\mu' = 0$, $\chi = 90°$, and $\chi' = 0°$.

in a single scattering of the incident unpolarized radiation by the lithium atoms. In the solar case, the combined theory finds applications in modeling of spectral lines like lithium 6708 Å for which the effects of both fine and hyperfine structure are significant.

In the absence of magnetic fields, we recover the results already published by Belluzzi et al. (2009). In the present paper, we illustrate the effects of a deterministic magnetic field on the Stokes profiles of the lithium D line system. We cover the entire field strength regime from a weak field Hanle regime to incomplete and complete PB regimes. When the fields are weak, the Stokes profiles exhibit the well-known Hanle signatures at the centers of the lithium D lines, namely, depolarization of Q/I and rotation of polarization plane. We note that there are Zeeman-like signatures for stronger fields. We show the signatures of level-crossings and avoided crossings in Stokes profiles and polarization diagrams. Unlike the pure J state or F state interferences, when J and F state interferences are treated together, a multitude of level-crossings and avoided crossings occur which produce multiple loops in the polarization diagrams and interesting signatures in the U/I profiles. Non-zero NCP is seen for fields in the incomplete PB regime which arises not only due to nonlinear MS but also due to the A-O conversion mechanism as already described in LL04. However, its diagnostic potential needs to be explored. We perform the calculations including the effects of PRD. However, its effect manifests only when one considers the transfer of the line radiation in the solar atmospheric conditions.

We thank the referee for very useful, detailed, constructive comments and suggestions which helped us understand the results better and improve the paper substantially. We acknowledge the use of the HYDRA cluster facility at the Indian Institute of Astrophysics for the numerical computations related to the work presented in this paper.

APPENDIX A
THE MAGNETIC REDISTRIBUTION FUNCTIONS FOR THE COMBINED J AND F STATE INTERFERENCES

The magnetic redistribution functions of type-II in the case of combined J and F state interferences have the same form as those in cases where only the interferences between fine structure or hyperfine structure states are considered, except for the increase in the dimension of the quantum number space. For our problem of interest, they take the forms given by

$$R^{\mathrm{II,H}}_{k_b\mu_b k_a\mu_a k_f\mu_f}\left(x_{ba}, x'_{ba}, \Theta\right) = \frac{1}{\pi \sin\Theta} \exp\left\{-\left[\frac{x_{ba} - x'_{ba} + x_{k_a\mu_a k_f\mu_f}}{2\sin(\Theta/2)}\right]^2\right\} \times H\left(\frac{a}{\cos(\Theta/2)}, \frac{x_{ba} + x'_{ba} + x_{k_a\mu_a k_f\mu_f}}{2\cos(\Theta/2)}\right), \quad (14)$$

and

$$R^{\mathrm{II,F}}_{k_b\mu_b k_a\mu_a k_f\mu_f}\left(x_{ba}, x'_{ba}, \Theta\right) = \frac{1}{\pi \sin\Theta} \exp\left\{-\left[\frac{x_{ba} - x'_{ba} + x_{k_a\mu_a k_f\mu_f}}{2\sin(\Theta/2)}\right]^2\right\} \times 2F\left(\frac{a}{\cos(\Theta/2)}, \frac{x_{ba} + x'_{ba} + x_{k_a\mu_a k_f\mu_f}}{2\cos(\Theta/2)}\right). \quad (15)$$

Here, Θ is the scattering angle, and the functions H and F are the Voigt and Faraday–Voigt functions (see Equation (18) of Smitha et al. 2011). The quantities appearing in the expressions for the type-II redistribution functions have the following definitions:

$$x_{ba} = \frac{\nu_{k_b\mu_b k_a\mu_a} - \nu}{\Delta\nu_{\mathrm{D}}};\ x'_{ba} = \frac{\nu_{k_b\mu_b k_a\mu_a} - \nu'}{\Delta\nu_{\mathrm{D}}};$$
$$x_{k_a\mu_a k_f\mu_f} = \frac{\nu_{k_a\mu_a k_f\mu_f}}{\Delta\nu_{\mathrm{D}}};\ a = \frac{\gamma}{4\pi\Delta\nu_{\mathrm{D}}}, \quad (16)$$

where x_{ba} is the emission frequency, x'_{ba} is the absorption frequency, a is the damping parameter, and $\Delta\nu_{\mathrm{D}}$ is the Doppler width.

The auxiliary functions h^{II} and f^{II} appearing in Equation (12) can be constructed by making use of Equations (14) and (15) as

$$\left(h^{\mathrm{II}}_{k_b\mu_b,k_{b'}\mu_{b'}}\right)_{k_a\mu_a k_f\mu_f} = \frac{1}{2}\left[R^{\mathrm{II,H}}_{k_b\mu_b k_a\mu_a k_f\mu_f} + R^{\mathrm{II,H}}_{k_{b'}\mu_{b'},k_a\mu_a k_f\mu_f}\right], \quad (17)$$

$$\left(f^{\mathrm{II}}_{k_b\mu_b,k_{b'}\mu_{b'}}\right)_{k_a\mu_a k_f\mu_f} = \frac{1}{2}\left[R^{\mathrm{II,F}}_{k_{b'}\mu_{b'},k_a\mu_a k_f\mu_f} - R^{\mathrm{II,F}}_{k_b\mu_b k_a\mu_a k_f\mu_f}\right]. \quad (18)$$

These auxiliary functions contain the information regarding the Doppler redistribution of photon frequencies.

APPENDIX B
THE PSS

The PSS is a basic test for checking the correctness of the eigenvalues and eigenvectors obtained from a diagonalization procedure, for a given problem. A detailed description of the PSS is given in LL04 (see pp. 321–325). In LL04, the manifestations of PSS are given separately for (a) a two-level atom with hyperfine structure and (b) a two-term atom exhibiting only FS. In this appendix, we formulate the PSS for the case of a two-term atom exhibiting both FS and HFS. We basically follow the same procedure as described in LL04 to derive the expression for the centers of gravity in frequency of the magnetic components.

The strengths of the magnetic components are given by

$$\mathcal{S}^{k_a\mu_a,k_b\mu_b}_q = \left|\langle L_a SI_s, k_a\mu_a|\mathrm{r}_q\,|L_b SI_s, k_b\mu_b\rangle\right|^2, \quad (19)$$

which are essentially the square of the complex amplitude of the transition between the lower term (quantities with subscripts a) and the upper term (quantities with subscripts b). r_q are the spherical components of the dipole moment operator. Using the basis expansion defined in Equation (4), the Wigner–Eckart theorem and its corollary, we expand the above equation as

$$\mathcal{S}^{k_a\mu_a,k_b\mu_b}_q = (2L_a+1) \times \sum_{J_aJ_{a'}J_bJ_{b'}F_aF_{a'}F_bF_{b'}} (-1)^{J_a+J_{a'}+J_b+J_{b'}} \times C^{k_a}_{J_aF_a}(L_aSI_s,\mu_a)C^{k_a}_{J_{a'}F_{a'}}(L_aSI_s,\mu_a) \times C^{k_b}_{J_bF_b}(L_bSI_s,\mu_b)C^{k_b}_{J_{b'}F_{b'}}(L_bSI_s,\mu_b) \times \sqrt{(2J_a+1)(2J_{a'}+1)(2J_b+1)(2J_{b'}+1)(2F_a+1) \times (2F_{a'}+1)(2F_b+1)(2F_{b'}+1)} \times \begin{Bmatrix} L_a & L_b & 1 \\ J_b & J_a & S \end{Bmatrix}\begin{Bmatrix} L_a & L_b & 1 \\ J_{b'} & J_{a'} & S \end{Bmatrix}\begin{Bmatrix} J_a & J_b & 1 \\ F_b & F_a & I_s \end{Bmatrix} \times \begin{Bmatrix} J_{a'} & J_{b'} & 1 \\ F_{b'} & F_{a'} & I_s \end{Bmatrix}\begin{pmatrix} F_b & F_a & 1 \\ -\mu_b & \mu_a & -q \end{pmatrix}\begin{pmatrix} F_{b'} & F_{a'} & 1 \\ -\mu_b & \mu_a & -q \end{pmatrix} \times |\langle L_a||\mathbf{r}||L_b\rangle|^2, \quad (20)$$

with, $q = 0$ for π, $+1$ for σ_r, and -1 for the σ_b components. The transitions connecting the upper and the lower terms obey the selection rules $\Delta L = 0,\ \pm 1$, $\Delta S = 0$, $\Delta I_s = 0$, and $\Delta\mu = \mu_b - \mu_a = 0,\ \pm 1$. Summing the expression for the unnormalized strengths over all of the possible transitions, making use of the orthogonality property of the C-coefficients given in Equation (5a) of Casini & Manso Sainz (2005) and Equations (2.23a) and (2.39) of LL04, we obtain

$$\sum_{k_ak_b\mu_a\mu_b} \mathcal{S}^{k_a\mu_a,k_b\mu_b}_q = \frac{1}{3}(2L_a+1)(2S+1) \times (2I_s+1)\,|\langle L_a||\mathbf{r}||L_b\rangle|^2. \quad (21)$$

Making use of the condition that

$$\sum_{k_ak_b\mu_a\mu_b} \mathcal{S}^{k_a\mu_a,k_b\mu_b}_q = 1, \quad (22)$$

we write the expression for the normalized strengths as

$$\mathcal{S}^{k_a\mu_a,k_b\mu_b}_q = \frac{3}{(2S+1)(2I_s+1)} \times \sum_{J_aJ_{a'}J_bJ_{b'}F_aF_{a'}F_bF_{b'}} (-1)^{J_a+J_{a'}+J_b+J_{b'}} \times C^{k_a}_{J_aF_a}(L_aSI_s,\mu_a)C^{k_a}_{J_{a'}F_{a'}}(L_aSI_s,\mu_a) \times C^{k_b}_{J_bF_b}(L_bSI_s,\mu_b)C^{k_b}_{J_{b'}F_{b'}}(L_bSI_s,\mu_b) \times \sqrt{(2J_a+1)(2J_{a'}+1)(2J_b+1)(2J_{b'}+1) \times (2F_a+1)(2F_{a'}+1)(2F_b+1)(2F_{b'}+1)} \times \begin{Bmatrix} L_a & L_b & 1 \\ J_b & J_a & S \end{Bmatrix}\begin{Bmatrix} L_a & L_b & 1 \\ J_{b'} & J_{a'} & S \end{Bmatrix} \times \begin{Bmatrix} J_a & J_b & 1 \\ F_b & F_a & I_s \end{Bmatrix}\begin{Bmatrix} J_{a'} & J_{b'} & 1 \\ F_{b'} & F_{a'} & I_s \end{Bmatrix} \times \begin{pmatrix} F_b & F_a & 1 \\ -\mu_b & \mu_a & -q \end{pmatrix}\begin{pmatrix} F_{b'} & F_{a'} & 1 \\ -\mu_b & \mu_a & -q \end{pmatrix}. \quad (23)$$

The centers of gravity in frequency of the magnetic components are defined as

$$\Delta\nu_q = \sum_{k_a k_b \mu_a \mu_b} \mathcal{S}_q^{k_a\mu_a,k_b\mu_b} \Delta\nu_{\mu_a\mu_b}^{k_a k_b}, \tag{24}$$

with

$$\Delta\nu_{\mu_a\mu_b}^{k_a k_b} = \frac{E_{k_b}(L_b S I_s,\, \mu_b) - E_{k_a}(L_a S I_s,\, \mu_a)}{h}. \tag{25}$$

Using Equations (23) and (25) in Equation (24), and performing sums over k_a and k_b with the help of Equations (5a) and (7) of Casini & Manso Sainz (2005), we obtain

$$\begin{aligned}
\Delta\nu_q = {} & \frac{1}{h}\frac{3}{(2S+1)(2I_s+1)} \\
& \times \sum_{J_a J_{a'} J_b J_{b'} F_a F_{a'} F_b F_{b'} \mu_a \mu_b} (-1)^{J_a+J_{a'}+J_b+J_{b'}} \\
& \times \sqrt{\begin{array}{l}(2J_a+1)(2J_{a'}+1)(2J_b+1)(2J_{b'}+1) \\ \quad\times (2F_a+1)(2F_{a'}+1)(2F_b+1)(2F_{b'}+1)\end{array}} \\
& \times \begin{Bmatrix} L_a & L_b & 1 \\ J_b & J_a & S \end{Bmatrix} \begin{Bmatrix} L_a & L_b & 1 \\ J_{b'} & J_{a'} & S \end{Bmatrix} \begin{Bmatrix} J_a & J_b & 1 \\ F_b & F_a & I_s \end{Bmatrix} \\
& \times \begin{Bmatrix} J_{a'} & J_{b'} & 1 \\ F_{b'} & F_{a'} & I_s \end{Bmatrix} \begin{pmatrix} F_b & F_a & 1 \\ -\mu_b & \mu_a & -q \end{pmatrix} \begin{pmatrix} F_{b'} & F_{a'} & 1 \\ -\mu_b & \mu_a & -q \end{pmatrix} \\
& \times \Big[\delta_{J_a J_{a'}} \delta_{F_a F_{a'}} \langle L_b S J_b I_s F_b \mu_b | \mathcal{H}_T \, | L_b S J_{b'} I_s F_{b'} \mu_b \rangle \\
& - \delta_{J_b J_{b'}} \delta_{F_b F_{b'}} \langle L_a S J_a I_s F_a \mu_a | \mathcal{H}_T \, | L_a S J_{a'} I_s F_{a'} \mu_a \rangle \Big].
\end{aligned} \tag{26}$$

We separate the atomic and magnetic Hamiltonians in the above expression. It can be shown that the atomic part does not contribute to the centers of gravity. Using Equations (2.42), (2.41), (2.36d), (2.26d), and (2.39) of LL04, we simplify the magnetic Hamiltonian part and find that

$$\Delta\nu_q = -q\nu_{\rm L}, \tag{27}$$

where $\nu_{\rm L}$ is the Larmor frequency associated with the applied magnetic field. This result is the same as Equation (3.66) of LL04 which one would expect for a two-term atom without any fine or hyperfine structure. This means that the centers of gravity of the magnetic components in the PB regime have the same frequencies as the individual components due to Zeeman effect that would arise from the transitions between spinless lower and upper terms. In situations where the electron and nuclear spins are negligible, this is expected from the PSS.

We then verify that the eigenvalues and eigenvectors obtained by diagonalizing $\mathcal{H}_T$, when used in Equation (24), give the same value for $\Delta\nu_q$ as that calculated from Equation (27).

APPENDIX C
A-O CONVERSION MECHANISM

The RM presented in Equation (12) can be reduced to the phase matrix by integrating the auxiliary functions over the incoming and outgoing frequencies. The phase matrix will then take the form given by

$$P_{ij}(\boldsymbol{n}, \boldsymbol{n}'; \boldsymbol{B}) = \sum_{KK'Q} W_{KK'Q}(\boldsymbol{B})(-1)^Q \times \mathcal{T}^K_Q(i, \boldsymbol{n}) \mathcal{T}^{K'}_{-Q}(j, \boldsymbol{n}'), \tag{28}$$

where

$$\begin{aligned}
W_{KK'Q}(\boldsymbol{B}) = {} & \frac{3(2L_b+1)}{(2S+1)(2I_s+1)} \\
& \times \begin{Bmatrix} 1 & 1 & K \\ L_b & L_b & L_a \end{Bmatrix} \begin{Bmatrix} 1 & 1 & K' \\ L_b & L_b & L_a \end{Bmatrix} \\
& \times \sum_{J_b J_{b'} J_{b''} J_{b'''} F_b F_{b'} F_{b''} F_{b'''}} \\
& \times \sum_{\mu_b \mu_{b'}} (-1)^{J_b+J_{b'}+J_{b''}+J_{b'''}} (-1)^{K+K'} \\
& \times \sqrt{\begin{array}{l}(2J_b+1)(2J_{b'}+1)(2J_{b''}+1)(2J_{b'''}+1) \\ \quad\times (2F_b+1)(2F_{b'}+1)(2F_{b''}+1)(2F_{b'''}+1)\end{array}} \\
& \times \begin{Bmatrix} L_b & L_b & K \\ J_b & J_{b'} & S \end{Bmatrix} \begin{Bmatrix} L_b & L_b & K' \\ J_{b''} & J_{b'''} & S \end{Bmatrix} \\
& \times \begin{Bmatrix} J_{b'} & J_b & K \\ F_b & F_{b'} & I_s \end{Bmatrix} \begin{Bmatrix} J_{b'''} & J_{b''} & K' \\ F_{b''} & F_{b'''} & I_s \end{Bmatrix} \\
& \times \begin{pmatrix} F_b & F_{b'} & K \\ -\mu_b & \mu_{b'} & -Q \end{pmatrix} \begin{pmatrix} F_{b''} & F_{b'''} & K' \\ -\mu_b & \mu_{b'} & -Q \end{pmatrix} \\
& \times \sqrt{(2K+1)(2K'+1)} \sum_{k_b k_{b'}} C^{k_b}_{J_b F_b}(L_b S I_s,\, \mu_b) C^{k_b}_{J_{b''} F_{b''}} \\
& \times (L_b S I_s,\, \mu_b) C^{k_{b'}}_{J_{b'} F_{b'}}(L_b S I_s,\, \mu_{b'}) C^{k_{b'}}_{J_{b''} F_{b'''}}(L_b S I_s,\, \mu_{b'}) \\
& \times \frac{1}{1 + 2\pi i \nu(k_{b'}\mu_{b'},\, k_b\mu_b)/A(L_a S I_s \to L_b S I_s)}.
\end{aligned} \tag{29}$$

Here, A is the Einstein coefficient for the $L_a \to L_b$ transition and $\nu(k_{b'}\mu_{b'},\, k_b\mu_b) = (E_{k_{b'}\mu_{b'}} - E_{k_b\mu_b})/h$. We compute the $\mathcal{T}^K_Q$s for the geometry considered in Section 4.3 so that we can obtain an expression for the frequency integrated fractional circular polarization, $\tilde{p}_V$, similar to the one given in Section 10.20 of LL04. The explicit expressions for $\mathcal{T}^K_Q(i, \boldsymbol{n})$ in the atmospheric reference frame for a rotation of the form $R \equiv (0, -\theta, -\chi) \times (\chi_B, \theta_B, 0)$ are given by

$$\begin{aligned}
& \mathcal{T}^0_0(0, \boldsymbol{n}) = 1, \\
& \mathcal{T}^1_0(0, \boldsymbol{n}) = 0, \\
& \mathcal{T}^1_1(0, \boldsymbol{n}) = 0, \\
& \mathcal{T}^2_0(0, \boldsymbol{n}) = \frac{1}{\sqrt{2}} \Big[\frac{1}{4} \left(3\cos^2\theta - 1\right)\left(3\cos^2\theta_B - 1\right) \\
& \qquad + 3 \sin\theta \cos\theta \sin\theta_B \cos\theta_B \cos(\chi - \chi_B) \\
& \qquad + \frac{3}{4} \sin^2\theta \sin^2\theta_B \cos 2(\chi - \chi_B) \Big], \\
& \mathcal{T}^2_1(0, \boldsymbol{n}) = \frac{1}{\sqrt{2}} \Big[\frac{\sqrt{3}}{2\sqrt{2}} \left(3\cos^2\theta - 1\right) \sin\theta_B \cos\theta_B \\
& \qquad - \frac{\sqrt{3}}{\sqrt{2}} \sin\theta \cos\theta \Big[e^{i(\chi - \chi_B)} \Big(\cos\theta_B - \frac{1}{2} \Big)
\end{aligned}$$

$$\times \left(\cos\theta_B + 1\right) - \mathrm{e}^{-\mathrm{i}(\chi-\chi_B)}\left(\cos\theta_B + \frac{1}{2}\right)$$
$$\times \left(1 - \cos\theta_B\right)\Big] - \frac{\sqrt{3}}{2\sqrt{8}}\sin^2\theta\,\sin\theta_B$$
$$\times \Big[\mathrm{e}^{2\mathrm{i}(\chi-\chi_B)}\left(1 + \cos\theta_B\right)$$
$$- \mathrm{e}^{-2\mathrm{i}(\chi-\chi_B)}\left(1 - \cos\theta_B\right)\Big]\Big],$$

$$\mathcal{T}^2_2(0,\boldsymbol{n}) = \frac{1}{\sqrt{2}}\Bigg[\frac{\sqrt{3}}{4\sqrt{2}}\left(3\cos^2\theta - 1\right)\sin^2\theta_B$$
$$- \frac{\sqrt{3}}{2\sqrt{2}}\sin\theta\,\cos\theta\,\sin\theta_B\Big[\mathrm{e}^{\mathrm{i}(\chi-\chi_B)}$$
$$\times \left(1 + \cos\theta_B\right) - \mathrm{e}^{-\mathrm{i}(\chi-\chi_B)}\left(1 - \cos\theta_B\right)\Big]$$
$$+ \frac{\sqrt{3}}{8\sqrt{2}}\sin^2\theta\Big[\mathrm{e}^{2\mathrm{i}(\chi-\chi_B)}\left(1 + \cos\theta_B\right)^2$$
$$+ \mathrm{e}^{-2\mathrm{i}(\chi-\chi_B)}\left(1 - \cos\theta_B\right)^2\Big]\Bigg], \tag{30}$$

$$\mathcal{T}^0_0(1,\boldsymbol{n}) = 0,$$
$$\mathcal{T}^1_0(1,\boldsymbol{n}) = 0,$$
$$\mathcal{T}^1_1(1,\boldsymbol{n}) = 0,$$
$$\mathcal{T}^2_0(1,\boldsymbol{n}) = -\frac{\sqrt{3}}{2}\Bigg[\frac{\sqrt{3}}{\sqrt{8}}\sin^2\theta\left(3\cos^2\theta_B - 1\right)$$
$$- \frac{2\sqrt{3}}{\sqrt{2}}\sin\theta\,\cos\theta\,\sin\theta_B\,\cos\theta_B\,\cos(\chi-\chi_B)$$
$$+ \frac{\sqrt{3}}{\sqrt{8}}\left(1 + \cos^2\theta\right)\sin^2\theta_B\,\cos 2(\chi-\chi_B)\Bigg],$$
$$\mathcal{T}^2_1(1,\boldsymbol{n}) = -\frac{\sqrt{3}}{2}\Bigg[\frac{3}{2}\sin^2\theta\,\sin\theta_B\,\cos\theta_B$$
$$+ \sin\theta\,\cos\theta\Big[\mathrm{e}^{\mathrm{i}(\chi-\chi_B)}\left(\cos\theta_B - \frac{1}{2}\right)\left(\cos\theta_B + 1\right)$$
$$- \mathrm{e}^{-\mathrm{i}(\chi-\chi_B)}\left(\cos\theta_B + \frac{1}{2}\right)\left(1 - \cos\theta_B\right)\Big]$$
$$- \frac{1}{4}\left(1 + \cos^2\theta\right)\sin\theta_B\Big[\mathrm{e}^{2\mathrm{i}(\chi-\chi_B)}\left(1 + \cos\theta_B\right)$$
$$- \mathrm{e}^{-2\mathrm{i}(\chi-\chi_B)}\left(1 - \cos\theta_B\right)\Big]\Bigg],$$
$$\mathcal{T}^2_2(1,\boldsymbol{n}) = -\frac{\sqrt{3}}{2}\Bigg[\frac{3}{4}\sin^2\theta\,\sin^2\theta_B$$
$$+ \frac{1}{2}\sin\theta\,\cos\theta\,\sin\theta_B\Big[\mathrm{e}^{\mathrm{i}(\chi-\chi_B)}\left(1 + \cos\theta_B\right)$$
$$- \mathrm{e}^{-\mathrm{i}(\chi-\chi_B)}\left(1 - \cos\theta_B\right)\Big]$$
$$+ \frac{1}{8}\left(1 + \cos^2\theta\right)\Big[\mathrm{e}^{2\mathrm{i}(\chi-\chi_B)}\left(1 + \cos\theta_B\right)^2$$
$$+ \mathrm{e}^{-2\mathrm{i}(\chi-\chi_B)}\left(1 - \cos\theta_B\right)^2\Big]\Bigg], \tag{31}$$

$$\mathcal{T}^0_0(2,\boldsymbol{n}) = 0,$$
$$\mathcal{T}^1_0(2,\boldsymbol{n}) = 0,$$
$$\mathcal{T}^1_1(2,\boldsymbol{n}) = 0,$$
$$\mathcal{T}^2_0(2,\boldsymbol{n}) = \frac{\sqrt{3}}{2}\Big[-\sqrt{6}\,\sin\theta\,\sin\theta_B\,\cos\theta_B\,\sin(\chi-\chi_B)$$
$$+ \frac{\sqrt{3}}{\sqrt{2}}\cos\theta\,\sin^2\theta_B\,\sin 2(\chi-\chi_B)\Big],$$
$$\mathcal{T}^2_1(2,\boldsymbol{n}) = -\,\mathrm{i}\frac{\sqrt{3}}{2}\Bigg[\sin\theta\Big[\mathrm{e}^{\mathrm{i}(\chi-\chi_B)}\left(\cos\theta_B - \frac{1}{2}\right)\left(\cos\theta_B + 1\right)$$
$$+ \mathrm{e}^{-\mathrm{i}(\chi-\chi_B)}\left(\cos\theta_B + \frac{1}{2}\right)\left(1 - \cos\theta_B\right)\Big]$$
$$- \frac{1}{2}\cos\theta\,\sin\theta_B\Big[\mathrm{e}^{2\mathrm{i}(\chi-\chi_B)}\left(1 + \cos\theta_B\right)$$
$$+ \mathrm{e}^{-2\mathrm{i}(\chi-\chi_B)}\left(1 - \cos\theta_B\right)\Big]\Bigg],$$
$$\mathcal{T}^2_2(2,\boldsymbol{n}) = -\,\mathrm{i}\frac{\sqrt{3}}{2}\Bigg[\frac{1}{2}\sin\theta\,\sin\theta_B\Big[\mathrm{e}^{\mathrm{i}(\chi-\chi_B)}\left(1 + \cos\theta_B\right)$$
$$+ \mathrm{e}^{-\mathrm{i}(\chi-\chi_B)}\left(1 - \cos\theta_B\right)\Big]$$
$$+ \frac{1}{4}\cos\theta\Big[\mathrm{e}^{2\mathrm{i}(\chi-\chi_B)}\left(1 + \cos\theta_B\right)^2$$
$$- \mathrm{e}^{-2\mathrm{i}(\chi-\chi_B)}\left(1 - \cos\theta_B\right)^2\Big]\Bigg], \tag{32}$$

and

$$\mathcal{T}^0_0(3,\boldsymbol{n}) = 0,$$
$$\mathcal{T}^1_0(3,\boldsymbol{n}) = \frac{\sqrt{3}}{\sqrt{2}}\Big[\cos\theta\,\cos\theta_B$$
$$+ \sin\theta\,\sin\theta_B\,\cos(\chi-\chi_B)\Big],$$
$$\mathcal{T}^1_1(3,\boldsymbol{n}) = \frac{\sqrt{3}}{\sqrt{2}}\Bigg[\frac{1}{\sqrt{2}}\cos\theta\,\sin\theta_B - \frac{1}{2\sqrt{2}}\sin\theta\Big[\mathrm{e}^{\mathrm{i}(\chi-\chi_B)}$$
$$\times \left(1 + \cos\theta_B\right) - \mathrm{e}^{-\mathrm{i}(\chi-\chi_B)}\left(1 - \cos\theta_B\right)\Big]\Bigg],$$
$$\mathcal{T}^2_0(3,\boldsymbol{n}) = 0,$$
$$\mathcal{T}^2_1(3,\boldsymbol{n}) = 0,$$
$$\mathcal{T}^2_2(3,\boldsymbol{n}) = 0. \tag{33}$$

We then expand the summations over K, K', and Q in Equation (28) and write down the expressions for the P_{00} and P_{33} elements. We substitute in the expressions for P_{00} and P_{33} the $\mathcal{T}^K_Q$s evaluated for the incoming and outgoing rays by making use of Equations (30) and (33) for the geometry considered in Section 4.3. After elaborate algebra, we finally arrive at an expression for the frequency integrated fractional circular polarization given by

$$\tilde{p}_V = \frac{-2\sqrt{6}\,W_{120}}{16 - W_{220} - 3\,\mathrm{Re}\left(W_{222}\right)}. \tag{34}$$

As discussed in Section 4.3 and in Section 10.20 of LL04, due to the double summations over K and K' in Equation (28) and due to the fact that the spherical tensors $\mathcal{T}^K_Q(3, \boldsymbol{n})$ are non-zero only when $K = 1$, orientation can be produced in the upper term even when circular polarization is not present in the incident radiation. This mechanism is therefore called the A-O conversion mechanism. We identify that the term with $K = 1$ in the numerator of Equation (34) is responsible for the A-O conversion mechanism. We have discussed the signatures of this mechanism in the Stokes V parameter in Section 4.

REFERENCES

Arimondo, E., Inguscio, M., & Violino, P. 1977, RvMP, 49, 31
Belluzzi, L., Landi Degl'Innocenti, E., & Trujillo Bueno, J. 2009, ApJ, 705, 218
Bommier, V. 1980, A&A, 87, 109
Brog, K. C., Eck, T. C., & Wieder, H. 1967, PhRv, 153, 91
Casini, R., Landi Degl'Innocenti, M., Manso Sainz, R., Landi Degl'Innocenti, E., & Landolfi, M. 2014, ApJ, 791, 94
Casini, R., & Manso Sainz, R. 2005, ApJ, 624, 1025
Landi Degl'Innocenti, E. 1982, SoPh, 79, 291
Landi Degl'Innocenti, E. 1984, SoPh, 91, 1
Landi Degl'Innocenti, E., Landi Degl'Innocenti, M., & Landolfi, M. 1997, in Proc. Forum THEMIS, Science with THEMIS, ed. N. Mein & S. Sahal Bréchot (Paris: Obs. Paris-Meudon), 59
Landi Degl'Innocenti, E., & Landolfi, M. 2004, Polarization in Spectral Lines (Dordrecht: Kluwer) (LL04)
Ortega, J. 1968, in Mathematical Methods for Digital Computers, ed. A. Ralston & H. S. Wilf (New York: Wiley), 94
Smitha, H. N., Sampoorna, M., Nagendra, K. N., & Stenflo, J. O. 2011, ApJ, 733, 4
Sowmya, K., Nagendra, K. N., Sampoorna, M., & Stenflo, J. O. 2014a, ApJ, 793, 71
Sowmya, K., Nagendra, K. N., Stenflo, J. O., & Sampoorna, M. 2014b, ApJ, 786, 150
Stenflo, J. O. 1994, Solar Magnetic Fields: Polarized Radiation Diagnostics (Dordrecht: Kluwer)
Stenflo, J. O. 1998, A&A, 338, 301
Stenflo, J. O. 2015, ApJ, 801, 70
Wieder, H., & Eck, T. G. 1967, PhRv, 153, 103